Cosmic symplectite recorded irradiation by nearby massive stars in the solar system's parent molecular cloud

Lionel Vacher, Ryan Ogliore, Clive Jones, Nan Liu, David Fike

▶ **To cite this version:**

Lionel Vacher, Ryan Ogliore, Clive Jones, Nan Liu, David Fike. Cosmic symplectite recorded irradiation by nearby massive stars in the solar system's parent molecular cloud. Geochimica et Cosmochimica Acta, 2021, 309, pp.135-150. 10.1016/j.gca.2021.06.026 . hal-04028499

HAL Id: hal-04028499
https://hal.science/hal-04028499v1

Submitted on 14 Mar 2023

HAL is a multi-disciplinary open access archive for the deposit and dissemination of scientific research documents, whether they are published or not. The documents may come from teaching and research institutions in France or abroad, or from public or private research centers.

L'archive ouverte pluridisciplinaire **HAL**, est destinée au dépôt et à la diffusion de documents scientifiques de niveau recherche, publiés ou non, émanant des établissements d'enseignement et de recherche français ou étrangers, des laboratoires publics ou privés.

Cosmic symplectite recorded irradiation by nearby massive stars in the solar system's parent molecular cloud

Lionel G. Vacher[1*], Ryan C. Ogliore[1], Clive Jones[2], Nan Liu[1] & David A. Fike[2]
[1]Department of Physics, Washington University in St. Louis, St. Louis, MO, USA
[2]Department of Earth and Planetary Sciences, Washington University in St. Louis, St. Louis, MO, USA
[*](Corresponding author: **l.vacher@wustl.edu**)

ABSTRACT

The Sun's astrophysical birth environment affected the formation and composition of the Solar System. Primitive meteorites display mass-independent oxygen isotope anomalies that were likely caused by ultraviolet (UV) photochemistry of CO gas-phase molecules, either *(i)* in the outer solar nebula by light from the young Sun or *(ii)* in the parent molecular cloud by light from nearby stars. However, measurements of oxygen isotopes alone cannot unambiguously constrain the UV spectrum of the source responsible for the photochemistry. Sulfur, with four stable isotopes, can be used as a more direct probe of the astrophysical environment of mass-independent photochemistry. Here, we report the *in situ* isotopic analysis of paired oxygen and sulfur isotope systematics in cosmic symplectite (COS), magnetite-pentlandite intergrowths, in the primitive ungrouped carbonaceous chondrite Acfer 094. We show that COS grains contain mass-independent sulfur isotope anomalies (weighted means of $\Delta^{33}S = +3.84 \pm 0.72‰$ and $\Delta^{36}S = -6.05 \pm 2.25‰$, 2SE) consistent with H_2S photochemistry by UV from massive O and B stars close to the Solar System's parent molecular cloud, and inconsistent with UV from the protosun. The presence of coupled mass-independent sulfur and oxygen ($\Delta^{17}O = 86 \pm 6‰$, 2SE) isotope anomalies in COS imply that these anomalies originated in the same astrophysical environment. We propose that this environment is the photodissociation region (PDR) of the Solar System's parent molecular cloud, where nearby massive stars irradiated the edge of the cloud. We conclude that the Sun's stellar neighbors, likely O and B stars in a massive-star-forming region, affected the composition of the Solar System's primordial building blocks.

KEYWORDS

Chondrites, Sulfur Isotopes, Photodissociation, Solar Nebula, Molecular Cloud

1. INTRODUCTION

Oxygen, with three stable isotopes (^{16}O, ^{17}O, and ^{18}O), is the third most abundant element in the Solar System and resided in gas, ice, and rocky material in the early Solar System. The oxygen isotopic composition of the Sun, which makes up 99% of the Solar System's mass, is ~6% enriched in ^{16}O compared to most of the rocky material that makes up the rest of the Solar System (McKeegan et al., 2011). On a $\delta^{17}O$ vs. $\delta^{18}O$ diagram (expressed as $\delta^{17,18}O = \{(^{17,18}O/^{16}O)/(^{17,18}O/^{16}O_{SMOW}) - 1\} \times 1000$; SMOW = Standard Mean Ocean Water), this dichotomy results in a mass-independent fractionation line with a slope ≈ 1, which has been interpreted as mixing between two distinct isotopic endmembers in the solar nebula: *(i)* the ^{16}O-rich solar gas and *(ii)* ^{16}O-poor H_2O (Clayton, 1979; McKeegan et al., 2011). The ^{16}O-poor (or, high $\Delta^{17}O = \delta^{17}O - 0.52 \times \delta^{18}O$) reservoir is thought to result from the CO self-shielding process—selective photodissociation of $C^{17,18}O$ at far-ultraviolet wavelengths that converted CO gas to ^{16}O-poor H_2O (e.g., Lyons and Young, 2005). CO self-shielding is observed astronomically in diffuse molecular clouds (Sheffer et al., 2002) and young stellar objects (Smith et al., 2009). To explain the Solar System's $\Delta^{17}O$ variability, CO self-shielding is proposed to have occurred either *(i)* in the inner or outer solar nebula by light from the young Sun (Clayton, 2002; Lyons and Young, 2005) or *(ii)* in the parent molecular cloud by light from nearby stars (Yurimoto and Kuramoto, 2004; Lee et al., 2008). Recent studies have shown that variable $\Delta^{17}O$ reservoirs may have predated Solar System formation because the irradiation time needed for the young Sun to create $\Delta^{17}O$ anomalies in the solar nebula is too long to explain $\Delta^{17}O$ variability among ^{26}Al-poor, grossite-rich Ca, Al-rich inclusions (CAIs) (Krot et al., 2006, 2020) and in the layers of a spinel-rich Ca, Al-rich spherule (Simon et al., 2019).

CO self-shielding models in nebular or molecular-cloud environments are able to reproduce a range of $\Delta^{17}O$, which includes the values measured in chondrite components (e.g., Lyons and Young, 2005; Young, 2007b; Lee et al., 2008; Lyons, 2014). The magnitude of $\Delta^{17}O$ produced in these models depends sensitively on the gas density, UV flux, and irradiation time (Adams, 2010)—all unknown parameters. Additionally, an inherited $\Delta^{17}O$ variability in the solar nebula could mean that either CO self-shielding created $\Delta^{17}O$ variability in the Solar System's parent molecular cloud, or the molecular cloud itself may have inherited these anomalies from prior astrophysical processes (Jacquet et al., 2019). For

these reasons, $\Delta^{17}O$ measurements and CO self-shielding models cannot unambiguously constrain the astrophysical source of the photochemical mass-independent isotopic signature in the Solar System.

Sulfur has four stable isotopes: ^{32}S, ^{33}S, ^{34}S and ^{36}S (isotope ratios are usually expressed as $\delta^{33}S$, $\delta^{34}S$, and $\delta^{36}S$ ($\delta^{x}S = \{(^{x}S/^{32}S)/(^{x}S/^{32}S_{V\text{-}CDT}) - 1\} \times 1000$; where x represents ^{33}S, ^{34}S or ^{36}S, and V−CDT: Vienna−Canyon Diablo Troilite). With four stable isotopes, S-bearing phases can record a range of mass-independent processes (Thiemens and Lin, 2019). Hydrogen sulfide (H_2S) is expected to be the most abundant sulfur-bearing gas-phase species in the solar nebula, cometary ice, and warm regions of the molecular cloud (Pasek et al., 2005; Calmonte et al., 2016; Rivière-Marichalar et al., 2019). Sulfur can experience mass-independent isotope fractionation by isotopologue-specific ultraviolet photolysis (Farquhar et al., 2000; Chakraborty et al., 2013). This process is different than self-shielding, which requires that the absorption spectrum of the molecule has narrow and well-separated lines so that the most abundant isotopologue saturates, reducing its dissociation rate compared to the rarer isotopologues. Gas-phase H_2S in the vacuum UV does not have narrow and well-separated lines, but undergoes mass-independent photolysis via predissociative processes (Chakraborty et al., 2013). UV-irradiated gaseous H_2S dissociates through five different branches (Schnieder et al., 1990) to elemental S^0 (Chakraborty et al., 2013). The contributions of the five branches will change depending on the UV wavelength. Isotopologues and different excited states of H_2S and SH have different accidental near-resonances between rovibrational levels, which can allow for access to "doorway states" to dissociation. This creates a mass-independent isotope selection in the photodissociation of H_2S where a larger fraction of some isotopologues are dissociated compared to others (Chakraborty et al., 2013; Zhou et al., 2020). As a given reservoir of gas-phase H_2S is irradiated by UV light, its abundance will decrease as H_2S undergoes photodissociation. The remaining H_2S will have a sulfur isotopic composition different from the starting composition (in a way that depends on the UV spectrum), with the complementary composition (by mass balance) in elemental S. For this isotopic anomaly to be preserved, the product S^0 must be kept separate from the remaining H_2S (similar to isotopically anomalous oxygen produced by CO self-shielding). Additionally, an isotope anomaly created by this process must take place in an environment with a UV flux sufficient to dissociate significant H_2S, but not so high as to dissociate all H_2S into S^0. Such a "Goldilocks" environment is similar to the environment needed for CO self-shielding to deplete photons able to dissociate $C^{16}O$, but not deplete

photons needed to dissociate $C^{17}O$ and $C^{18}O$. Isotope-selective photodissociation of H_2S and CO work in different ways, but both may operate in the same astrophysical environments.

Photolysis experiments of H_2S at the Lyman−α spectral line (Lyα, 121.6 nm) produce S^0 with mass-independent anomalies that define a $\Delta^{36}S/\Delta^{33}S$ ratio of −2.97 ± 0.73 (2σ) (Chakraborty et al., 2013) (where $\Delta^{33}S = \delta^{33}S - 1000 \times [(1 + \delta^{34}S / 1000)^{0.515} - 1]$) and $\Delta^{36}S = \delta^{36}S - 1000 \times [(1 + \delta^{34}S / 1000)^{1.89} - 1]$)). At wavelengths slightly larger and smaller than Lyα, the measured $\Delta^{36}S/\Delta^{33}S$ ratio is significantly more positive (Table S2, Chakraborty et al., 2013). Photodissociation of H_2S with UV close to Lyα yields a product SH fragment that populates the A $^2\Sigma^+$ excited state. At slightly larger and smaller wavelengths, the SH fragment populates the X $^2\Pi$ state (Schnieder et al., 1990). The two dissociation branches that produce SH fragments dominate at these wavelengths (Zhou et al., 2020). Both SH fragments undergo predissociation to make elemental S, but this predissociation is quantum-state dependent. Stars with neutral hydrogen in their atmosphere, such as young stars in their T Tauri phase, have strong emission at Lyα (Thalmann et al., 2010). Massive and hot O and B stars with no neutral hydrogen do not have a strong emission at Lyα (Heays et al., 2017). The photodissociation of H_2S, through a fortunate coincidence between H_2S photochemistry and stellar astrophysics, can serve to differentiate between massive stars and young T-Tauri stars as the astronomical source of isotope-selective photodissociation.

Analysis of paired oxygen and sulfur isotope systematics in cosmic symplectite (COS), a nanometer-scale intergrowth of magnetite (Fe_3O_4) and pentlandite ($[Fe,Ni]_9S_8$) (Seto et al., 2008), can provide unique insights into photochemical processing of Solar System materials. The signature of ^{16}O-poor H_2O is found in COS in the primitive ungrouped carbonaceous chondrite Acfer 094 (Sakamoto et al., 2007). Acfer 094 shows similarities to the most primitive asteroidal and cometary material in our collections: *(i)* ultra−porous lithologies that once contained ices, similar in morphology to chondritic-porous interplanetary dust particles (CP-IDPs) are found in Acfer 094 (Matsumoto et al., 2019); *(ii)* a symplectite assemblage of maghemite/pentlandite was found in the Stardust samples from comet 81P/Wild 2, similar in structure and chemical composition as COS, but not in oxygen isotopic composition (Nguyen et al., 2017); *(iii)* presolar grain abundances in Acfer 094 are relatively high, comparable with IDPs and the most primitive chondrites (Floss et al., 2013). Acfer 094's icy parent body may have formed in the outer Solar System, where it could have incorporated S-bearing ices like those detected in comets (Calmonte et al., 2016). Sulfur in COS, intimately associated at the

nanometer scale with the ^{16}O-poor product of photochemical processing, may provide insights into the astrophysical environment for the Solar System formation.

2. MATERIAL AND METHODS

2.1 Mounting of samples

The thin section of Acfer 094 (USNM 72337) was provided by the Smithsonian National Museum of Natural History. This section is mounted in an epoxy resin and was coated by ~30 nm of carbon for all the isotopic analyses. The polished section of Murchison used in this study was the same as report in Vacher et al., (2019). This section was coated by ~50 nm of gold to perform sulfur isotope analysis. The pyrrhotite standard was purchased on the internet from an individual seller and originated from the Nikolaeskiy mine (Dal'negorsk, Primorskiy Kray, Russia). Big fragments of pyrrhotite were first extracted from the sphalerite host, and small fresh fragments were crushed in powder for bulk sulfur isotope analysis. One of the biggest fragments was mounted in epoxy resin with a chip of the Balmat pyrite provided by the Department of Earth and Planetary Sciences at Washington University in St. Louis (USA). The section was then coated by ~50 nm of gold for sulfur isotope analysis.

2.2 Scanning Electron Microscope (SEM)

COS candidates were identified using a Scanning Electron Microscope (SEM) Tescan Mira3 FEG-SEM equipped with an EDAX Octane Plus energy dispersive X-ray (EDX) spectrometer at the Laboratory for Space Sciences, Washington University in St. Louis. SEM observations were performed with an accelerating voltage of 15 kV and 3 nA probe current. Based on their morphology and brightness in backscattered electrons (BSE), potential COS candidates were first identified from the survey of an ultra-high-resolution BSE mosaic of a thin section of Acfer 094 (~2×2 cm, 40,000 images and 50 nm/px) (Fig. S1). COS candidates that displayed consistent qualitative SEM-EDS analyses with the study of Sakamoto et al. (2007) were flagged for subsequent oxygen isotope analyses.

2.3 NanoSIMS oxygen isotopes analyses

Oxygen isotopic measurements on COS candidates were performed with the Cameca NanoSIMS 50 ion microprobe at Washington University in St. Louis. We used a ~1 pA Cs^+ primary beam focused to 100 nm. Secondary ion images of $^{16}O^-$, $^{17}O^-$ and $^{18}O^-$ were collected

simultaneously in multi-detection mode on electron multipliers (EMs) at a mass resolution power of ~6,000−10,000 (Cameca definition) for $^{17}O^-$ (using entrance and aperture slits #3), sufficient to resolve isobaric contribution of $^{16}OH^-$ to $^{17}O^-$, with the hydride contribution estimated to be <1‰. Prior to each measurement, the analyzed area was pre-sputtered for 25−30 min with a beam intensity of ~100 pA on a 15×15 μm area. Then, this primary beam was rastered over a 3×3μm area, divided into 128×128 pixels for isotopic analysis. We collected a total of 200 measurement cycles for a total analysis time of ~60 min (excluding pre-sputtering time) to achieve counting statistics of ~3‰ (2σ) for $\delta^{18}O$ and ~8‰ (2σ) for $\delta^{17}O$. The NanoSIMS image data were processed using L'image software (L. R. Nittler) and corrected for the deadtime of EMs. Oxygen isotopic ratios ($^{17}O/^{16}O$ and $^{18}O/^{16}O$) are reported as delta values relative to SMOW standard ($^{17}O/^{16}O_{SMOW} = 3.8290 \times 10^{-4}$ and $^{18}O/^{16}O_{SMOW} = 2.0052 \times 10^{-3}$; McKeegan et al., 2011 and references therein). Oxygen isotopic ratios of COS were corrected for instrumental mass fractionation (IMF), estimated from ten analyses of radial magnetite grains (Table S1) found in a dark clast of Acfer 094 (Fig. S2) and assumed to have the same mean composition of CI magnetite (i.e., $\delta^{18}O = 5 \pm 3$‰ and $\delta^{17}O = 4 \pm 2$‰; 2σ) reported in Rowe et al., (1994). Typical $^{16}O^-$ count rates were ~1×10^5 and ~2×10^5 cps for COS and magnetite, respectively. Total 2σ errors for each measurement (including internal statistical errors and external reproducibility of magnetite) were estimated to be ~6‰ for $\delta^{18}O$, ~18‰ for $\delta^{17}O$, and ~19‰ for $\Delta^{17}O$.

2.4 Bulk sulfur isotope analyses

Determination of the bulk $\delta^{34}S$ value of our internal standard pyrrhotite (from Russia) was performed using an ECS 4010 elemental analyzer (EA) (Costech, Valencia, CA, USA) coupled to a Delta V Plus isotope ratio mass-spectrometer (IRMS) (Thermo Scientific, Waltham, MA, USA) at Washington University in St. Louis. Four aliquots of powdered pyrrhotite (~125 μg) were loaded into tin capsules with 1–2 mg V_2O_5 and then combusted in the elemental analyzer. The $^{34}S/^{32}S$ ratios were then measured in a Delta V Plus IRMS and corrected to Vienna−Canyon Diablo Troilite standard (V-CDT) by bracketing analyses of in-house V-CDT-calibrated ZnS, BaS and $BaSO_4$ standards. The average sulfur content of the pyrrhotite was 37.8 ± 1.9 wt% (2σ), and its average $\delta^{34}S$ value was 2.9 ± 0.1‰ (2σ).

2.5 SIMS sulfur isotope analyses

Sulfur isotopic compositions of COS and Fe−Ni sulfides were measured with a Cameca IMS 7f-GEO at the Department of Earth and Planetary Sciences at Washington University in St. Louis. Due to the size difference between sulfide (~50 μm) and COS (~5−10 μm) grains, analyses were made using two different modes: spot mode for Fe-Ni sulfide (spot size of 10×10μm) and scanning ion imaging mode for COS (raster size of 20×20 or 10×10 μm; Fig. S3).

Spot mode: A Cs^+ primary ion beam (~4 μm of beam size) with a current of ~3 nA was used to collect $^{32}S^-$, $^{33}S^-$, $^{34}S^-$, $^{36}S^-$ secondary ions in monocollection mode using two faraday cups (10^{10} ohm resistor for FC1 and 10^{11} ohm resistor for FC2) and one EM. Charge compensation was applied using a normal-incident electron gun (e-gun). When measuring multiple sulfur isotopes, the MRP is set to ~3,900 to separate $^{33}S^-$ from the $^{32}SH^-$ ion. However, because the contribution of the $^{32}SH^-$ peak was higher on the unknown samples compared to the pyrrhotite standard, we adjusted the MRP ≈ 5,000 to resolve this interference on Fe−Ni sulfide and achieve maximum flatness on the top of the $^{32}S^-$ and $^{34}S^-$ peaks (ES = 30 μm). We also tested on $^{32}S^-$ ions collected on FC1, $^{33}S^-$ and $^{34}S^-$ ions on FC2 and $^{36}S^-$ ions on EM (raster size of 10×10). Background levels on FCs were recorded at every measurement and were typically ~3×10^4 c/s on FC1 and ~6×10^3 c/s on FC2. Presputtering over an area of ~12×12 μm was applied before each measurement for 100 s in order to remove carbon or gold coating at the surface of sulfide grains. Counting time was set to 0.96 s for each secondary ion (2s of waiting time to allow the magnet to switch), and beam blanking was applied to avoid over-sputtering during waiting times and quasi continuously monitor primary current. Measurements were repeated over 50 cycles (total measuring time of ~12 min) to achieve counting statistics of ~0.2‰ (2σ) for $\delta^{33}S$, ~0.1‰ (2σ) for $\delta^{34}S$, ~1.7‰ (2σ) for $\delta^{36}S$ on Fe−Ni sulfide. Isotope ratios are presented in permil (‰) relative to V−CDT standard (Ding et al., 2001). We measured two terrestrial standards to define the mass-dependent fractionation (MDF) line: *(i)* a pyrrhotite from Russia that was used as our internal standard ($\delta^{34}S_{V\text{-}CDT}$ = 2.9 ± 0.1‰; $^{32}S \approx 1.8 \times 10^8$ c/s) and *(ii)* a pyrite from Balmat ($\delta^{34}S_{V\text{-}CDT}$ = 15.1 ± 0.2‰; $^{32}S \approx 2.3 \times 10^8$ cps, Crowe and Vaughan, 1996). IMF for Fe−Ni sulfide was determined from our internal pyrrhotite standard. Analyses of sample unknowns were bracketed by measurements of standards before and after each group of different samples (Murchison and Acfer 094). IMF values of unknowns were then calculated by averaging the sulfur isotopic composition of the bracketed standards of each group of unknowns. The following corrections were applied to the data: *(i)* a dead-time correction and

(ii) time interpolation of $^{33}S^{-}$, $^{34}S^{-}$ and $^{36}S^{-}$counts to match the measurement time of $^{32}S^{-}$. Typical measurement errors (2σ) on Fe−Ni sulfide, accounting for statistical errors on each measurement and the external reproducibility of the standard, were estimated to be ~0.7‰ for $\delta^{33}S$, ~0.9‰ for $\delta^{34}S$, ~3.1‰ for $\delta^{36}S$, ~1.0‰ for $\Delta^{33}S$, and ~2.0‰ for $\Delta^{36}S$.

Ion imaging mode: all sulfur secondary ions were collected in monocollection mode using only the EM detector. A low Cs^{+} primary ion beam current of ~13 pA (~1 µm of beam size) was applied to collect $^{32}S^{-}$, $^{33}S^{-}$ and $^{34}S^{-}$ on EM. However, because at such low ion beam current the counting statistics of $^{36}S^{-}$ is extremely low, we separated the acquisition of $^{36}S^{-}$ from the acquisition of $^{32}S^{-}$, $^{33}S^{-}$ and $^{34}S^{-}$. Immediately after the determination of (1) $^{33}S/^{32}S$ and $^{34}S/^{32}S$ isotope ratios (raster sizes of 20×20 and 10 ×10 µm), we collected (2) $^{34}S^{-}$ and $^{36}S^{-}$ with a Cs^{+} primary ion beams of ~30−40 pA (~2 µm of beam size) to determine the $^{36}S/^{34}S$ isotope ratio. Finally, by multiplying together the mean $^{34}S/^{32}S$ isotope ratio from (1) and $^{36}S/^{34}S$ isotope ratio from (2), we determined the mean $^{36}S/^{32}S$ isotope ratio of standards and unknowns. We note that changing the analytical conditions between settings (1) and (2) could possibly modify the instrumental mass fractionation and, therefore, induce a systematic error. However, given that each isotopic ratio had been corrected for mass fractionation using data acquired from our internal pyrrhotite standard with the same analytical conditions as the unknown measurements (prior to the ratio multiplication), we do not expect a systematic error into the final data reduction. Also, because of the large size of COS1, we were able to run one spot mode analysis to compare our results between the two analysis modes for $\Delta^{36}S$ on the same COS grain. We found a consistent $\Delta^{36}S$ value within errors between the spot analysis ($\Delta^{36}S = -6.35 \pm 3.12$‰, 2σ) and the imaging analysis ($\Delta^{36}S = -5.04 \pm 5.05$‰, Table 2) for COS1, indicating that our correction for the $^{36}S/^{32}S$ ratio does not add a systematic error (see Supplementary Materials S1). Charge compensation was applied for every acquisition using an e-gun. Different analytical settings were applied for (1) $^{32}S^{-}$, $^{33}S^{-}$ and $^{34}S^{-}$: MRP = 6,000−9,000 (ES = 18 µm), counting time = 19.3 s, and acquisition of ~100 cycles and (2) $^{34}S^{-}$ and $^{36}S^{-}$: MRP = 4,000 (ES = 36 µm), counting time = 29.52 s, and acquisition of ~130 cycles. Data was processed using an in-house MATLAB code, and ROIs were defined in order to select pixels from only COS areas. Like for the spot mode, we used our internal pyrrhotite and the Balmat pyrite standards to define the MDF line. IMF of COS was calculated from our internal pyrrhotite standard. We note that our sample has a different matrix composition than our pyrrhotite standard and, therefore, a matrix effect should affect the isotopic correction of COS (see Supplementary Materials S1). However, this effect

(expected to be < 2‰) only affects the composition of the COS in a mass-dependent way and should not affect the mass-independent anomaly detected in COS. In addition, due to the long duration of each unknown measurement, a significant drift of the EM over the time was observed during the analytical session (with a larger effect on the heavy sulfur isotopes). Thus, each COS analysis was bracketed by typically three pyrrhotite standards before and after their analysis. Then, a unique IMF value for each COS was calculated by averaging the sulfur isotopic composition of the six bracketed standards. The following corrections were applied to the data: *(i)* a dead-time correction, *(ii)* a quasi-simultaneous arrival (QSA) effect correction, and *(iii)* the ^{32}SH hydride contribution correction (see Supplementary Materials S1).

Our ion probe measurements are subject to statistical uncertainty (counting statistics) and systematic uncertainties. The stability of the magnet and other varying analytical conditions can cause the measured isotope ratios to change. The systematic uncertainties can be estimated by measurements of standards and provide a minimum uncertainty bound on the standard error (repeated) measurement of the unknown. It is not useful to continue lowering the statistical uncertainty (with measurements of more COS grains) below the systematic uncertainty. To estimate the systematic uncertainty for sulfur isotopes, we calculated the reduced chi-squared (χ^2) of individual measurements compared to the weighted mean (i.e., Δ^{33}S and Δ^{36}S of each set) and associated p-value of six sets of five to six standard pyrrhotite measurements. We summed the χ^2 and degrees of freedom for each set to calculate a p-value for all six sets of standards. With only statistical uncertainties, we calculated a p-value of 0.58 for Δ^{33}S and 0.42 for Δ^{36}S. These p-values are reasonable and indicate that there is no major unaccounted systematic uncertainty. Next, we added an increasing systematic uncertainty in quadrature with the statistical uncertainty and recalculated χ^2 until the associated p-values reached 0.317. This is an estimate of the 1σ, one-sided upper bound of allowable systematic uncertainty. For Δ^{33}S, the maximum allowable uncertainty is 0.40, and for Δ^{36}S it is 0.60 (both 1σ). These values are comparable or a bit smaller than the standard error of our measurement (~0.36 and ~1.13 for Δ^{33}S and Δ^{36}S standard errors, respectively, Table 2). It would not be prudent to, for example, decrease the standard error by a factor of four by measuring 16 times as many COS grains, as we cannot constrain the standard error to be sufficiently small based on the reproducibility of our standards. To significantly increase the precision of the measurement of Δ^{33}S and Δ^{36}S in COS, a different technique is necessary.

3. RESULTS

3.1 Petrography and oxygen analyses of cosmic symplectite

Twenty-four COS grains were observed in the Acfer 094 section USNM 72337 (Fig. S1). The COS grains are scattered throughout the matrix of Acfer 094 and occur inside fractures (Fig. 1a–c). They are ~10–20 μm in width and ~10 μm in length and are sometimes accompanied or surrounded by elongated Fe,Ni–sulfides with fibrous textures (Fig. 1b–c, Abe et al., 2017). Secondary electron (SE) images of the COS surfaces after Cs^+ ion sputtering show the characteristic wormy-shaped structure of COS (Fig. 1d, Seto et al., 2008).

We selected eight largest COS grains for oxygen isotope analysis. Their measured $\delta^{17}O$ and $\delta^{18}O$ values range from 163 to 193‰ and 156 to 196‰, respectively (weighted mean of $\Delta^{17}O$ = 86 ± 6‰, 2SE) and plot along the slope ≈ 1 line, consistent with previous measurements within uncertainties (Sakamoto et al., 2007) (Fig. 2 and Table 1).

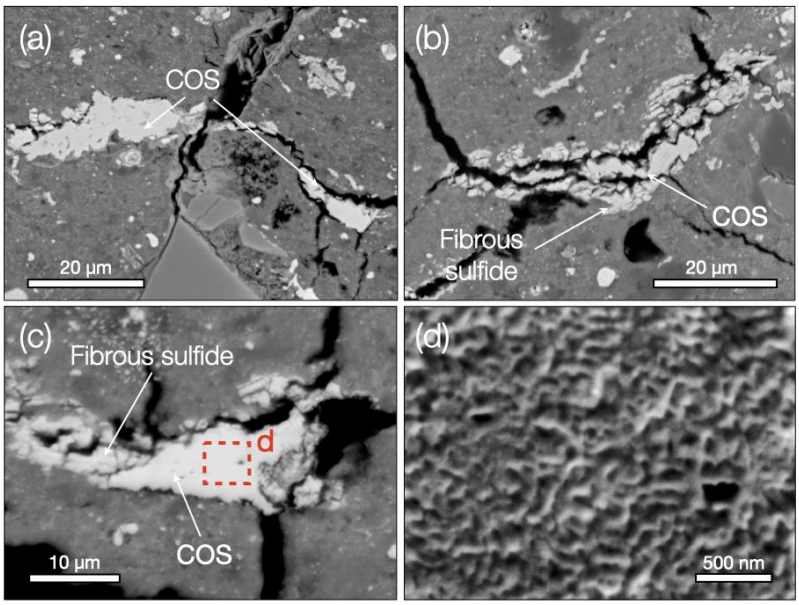

Fig. 1 Back-scattered electron (BSE) images of elongated COS grains within the matrix of Acfer 094 (a) free of sulfides and fully (b) or partially (c) surrounded by a rim of fibrous sulfides. Most of the COS grains are associated with fractures. (d) High-magnification SE image of the surface of the COS grain shown in panel (c) (delimited by red dashed lines) after the removal of most the carbon coating by Cs^+ ion sputtering during NanoSIMS analysis. The characteristic wormy-shaped structure of COS is visible.

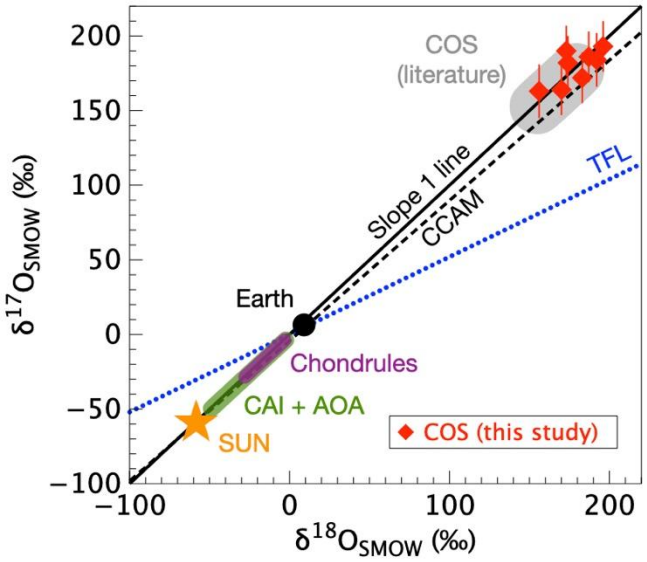

Fig. 2 $\delta^{17}O$ vs. $\delta^{18}O$ plot of COS measured in this study (red diamonds) compared with previous COS measurements, bulk Earth and other primary chondritic components (Sakamoto et al., 2007; McKeegan et al., 2011 and references therein). Uncertainties are 2σ. TFL: terrestrial fraction line; CCAM: carbonaceous chondrite anhydrous mineral line; AOA: amoeboid olivine aggregate.

3.2 Sulfur isotope analyses of cosmic symplectite and sulfide

Next, we measured the sulfur isotopic compositions of eleven COS grains where, for eight of them, oxygen isotopes were previously measured. All sulfur secondary ions were collected in the scanning ion imaging mode, and regions of interest (ROIs) were defined in order to select only pixels from COS areas (Fig. 3b−c). Their $\delta^{33}S$ and $\delta^{36}S$ are >10‰ larger than those of Fe−Ni sulfides reported in CM chondrites (Bullock et al. 2010) and deviate from the mass−dependent fractionation relationship (Fig. 3a). We obtained positive $\Delta^{33}S$ values between +1.91 and +6.35‰ (a weighted mean of +3.84 ± 0.72‰, 2SE) and near zero to negative $\Delta^{36}S$ values between −0.36 and −11.06‰ (a weighted mean of −6.05 ± 2.25‰, 2SE) (Table 2). For comparison, we also measured seven ~50 μm pyrrhotite grains in Acfer 094 and Murchison (CM2) in the spot mode and one pyrrhotite grain in the scanning ion imaging mode for comparison. These grains do not show mass-independent sulfur isotope anomalies within errors (weighted mean of $\Delta^{33}S$ = +0.20 ± 0.65 ‰ and $\Delta^{36}S$ = +0.53 ± 2.73‰, 2σ) and are consistent with the sulfides measured previously in CM chondrites (Bullock et al., 2010) (Fig. 3a and Table 3).

We assume that the COS we measured in Acfer 094 sampled a sulfur isotope reservoir that is characterized by a single $\Delta^{33}S$ value and a single $\Delta^{36}S$ value. That is, different grains of COS in Acfer 094 all sampled the same $\Delta^{33}S$−$\Delta^{36}S$ reservoir. This assumption is based on the

following observations: *(i)* COS shows remarkably consistent $\Delta^{17}O$ values (Fig. 2 and Table 1), *(ii)* sulfur and oxygen exist together in a symplectic assemblage of iron oxide/iron sulfide at the nanometer scale (Seto et al., 2008), and most importantly, *(iii)* we calculated the χ^2 and associated p-value of our COS data compared to the weighted means for $\Delta^{33}S$ and $\Delta^{36}S$. The p-values of 0.54 for $\Delta^{33}S$ and 0.13 for $\Delta^{36}S$ imply that our measured COS are consistent with being drawn from a single source reservoir of $\Delta^{33}S$ and $\Delta^{36}S$, within our measurement uncertainties. With these assumptions, the best estimate of the $\Delta^{33}S$ and $\Delta^{36}S$ values of the reservoir from which our measured COS were drawn is given by the weighted mean of our measurements, and our uncertainty in determining the reservoir $\Delta^{33}S$ and $\Delta^{36}S$ value is given by the standard error of our set of measurements.

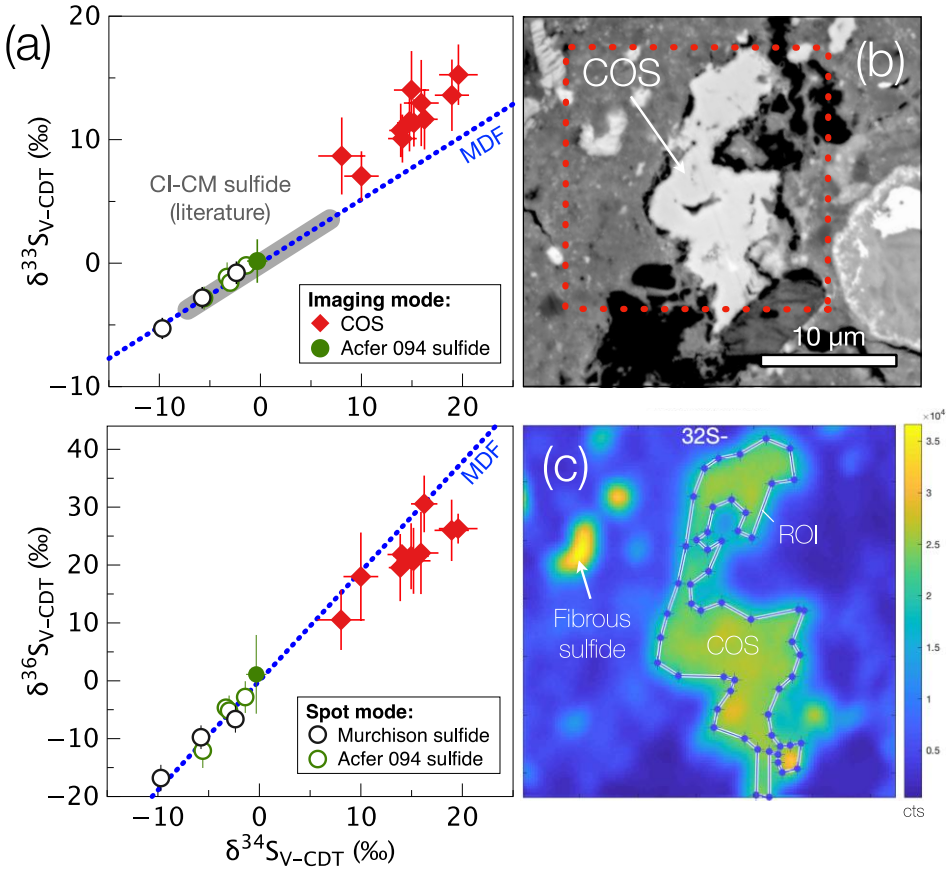

Fig. 3 (a) $\delta^{33}S$ vs. $\delta^{34}S$ and $\delta^{36}S$ vs. $\delta^{34}S$ plots of COS and sulfide grains (pyrrhotite) in Acfer 094 and Murchison (CM2) compared to CM sulfides from literature (Bullock et al., 2010). MDF: mass-dependent fractionation line. Uncertainties are 2σ. (b) BSE image of one COS grain (COS7) analyzed in this study. The red dotted (20×20 μm) square represents the SIMS analysis area for sulfur isotopes. (c) $^{32}S^-$ ion accumulated image for the area outlined by the red dotted square represented in panel b showing the ROI defined (line with dots) for COS7 for extracting pixels only from the COS grain.

4. DISCUSSION

4.1 Accretion of cometary S-bearing ice in Acfer 094's parent body?

Pentlandite and pyrrhotite in CI and CM chondrites are believed to form during hydrothermal alteration at low temperatures (Bullock et al., 2005; Kimura et al., 2011; Harries and Langenhorst, 2013; Schrader et al., 2016). Pentlandite is also present in hydrated IDPs but absent in anhydrous IDPs, suggesting that pentlandite was formed only by aqueous alteration (Zolensky and Thomas, 1995). The elongated texture of COS and fibrous sulfide are similar to fracture-filling veins of secondary carbonates and sulfides reported in aqueously altered CM chondrites and CM-like clasts, which is considered to be strong evidence of fluid circulation on an asteroidal parent body (Zolensky et al., 1996). Similarly, COS likely formed by aqueous alteration in Acfer 094's parent body from reaction between iron metal and ^{16}O-poor water (likely hosted in ultra-porous lithologies, Matsumoto et al., 2019). In Acfer 094, most of the metal is martensite with acicular texture and low nickel content (Kimura et al., 2008). One possibility is that the characteristic wormy-shaped structure of COS (Fig. 1d) might have originated from the corrosion of martensite (Sakamoto et al., 2007) by a fluid with sulfur activity. Equation 1 describes a possible chemical reaction for the formation of COS by parent body processing, as similarly suggested by (Palmer and Lauretta, 2011) for the alteration of kamacite exposed to water with limited sulfur activity:

$$4(Fe_{0.9}Ni_{0.1})\ [\text{martensite}] + S_{(aq)} + 3H_2O = (Fe_{0.6}Ni_{0.4})S\ [\text{pentlandite}] + Fe_3O_4\ [\text{magnetite}] + 4H_2 \quad (1)$$

The circulation of ^{16}O-poor fluid on the Acfer 094's parent body is supported by the oxygen isotopic composition of the Acfer 094's matrix that lies along the slope-1 line and correlates with the concentration of iron in the matrix (Vacher et al., 2020), a proxy of aqueous alteration degree (Leroux et al., 2015). The preservation of martensite – a sensitive mineral indicator of low peak temperature (Kimura et al., 2011) – in Acfer 094 and the distributions of iron and nickel in octahedral and tetrahedral sites of pentlandite, suggest that COS formed under low temperature conditions, likely below ~450 K (Seto et al., 2008). Acfer 094's parent body may have been heated by the decay of ^{26}Al ($t_{1/2}$ = 720,000 years) soon after it accreted, which resulted in hydrothermal alteration through the melting of the ^{16}O-poor water ice. Minimal degree of water-rock exchange between the ^{16}O-poor fluid and the ^{16}O-rich anhydrous matrix is needed to preserve the ^{16}O-poor isotopic composition of

^{16}O-poor magnetite (Young, 2007a). However, amorphous silicates are very susceptible to reaction with water (Guillou and Brearley, 2014), and isotopic equilibration between the ^{16}O-poor fluid and the ^{16}O-rich anhydrous matrix is expected to occur during the earliest stages of aqueous alteration. Assuming that aqueous alteration occurs essentially in a closed system, the range of oxygen isotopic compositions reported in COS ($\Delta^{17}O$ = 76−100‰) may have recorded this reaction path. The initial oxygen isotopic composition of the ^{16}O-poor H_2O reservoir, however, is likely much higher than the oxygen isotopic composition of COS, i.e., higher than ~100‰ in $\Delta^{17}O$.

In addition to anhydrous matrix, Fe−Ni sulfide grains (e.g., pyrrhotite or pentlandite) are prone to dissolution in CM chondrite (Singerling and Brearley, 2020) and thus represent a potential input of sulfur for the formation of COS. However, our sulfur isotopic compositions of Acfer 094's pyrrhotite exclude this possibility, as these sulfides do not show mass-independent sulfur isotope anomalies (Fig. 2a and Table 3). Alternatively, if Acfer 094's parent body accreted in the outer Solar System like comets as suggested in the literature (Matsumoto et al., 2019), then the mass-independent sulfur isotope anomalies released into the fluid likely originated from condensed S^0 or H_2S gas trapped into water ice grains (Palmer and Lauretta, 2011).

4.2 Mass-independent sulfur anomalies created by nebular photochemistry

Several cosmochemical mechanisms can cause mass-independent sulfur isotope anomalies in meteorites, such as *(i)* cosmic-ray spallation, *(ii)* stellar nucleosynthesis, *(iii)* decay of ^{36}Cl and *(iv)* nebular gas-phase photochemistry. Spallation reactions at the surface of Acfer 094's parent body can be ruled out because this process would affect both sulfide and COS sulfur isotopic compositions and produce positive $\Delta^{33}S$ and $\Delta^{36}S$ (Gao and Thiemens, 1991). A nucleosynthetic origin is unlikely, because the mass-independent sulfur anomalies observed in COS have not been seen in presolar grains (Hoppe et al., 2018), and a circumstellar/interstellar formation environment is not consistent with the mineralogy/petrology of COS. Decay of ^{36}Cl into ^{36}S from Cl-rich minerals is also excluded, since COS does not show any excess in ^{36}S (Fig. 3a and Table 2).

Modern and Archean terrestrial sulfate and sulfide minerals (Farquhar et al., 2013; Lin et al., 2018), as well as sulfides in Martian meteorites (Franz et al., 2014; Tomkins et al., 2020), display similar sulfur isotopic fractionation patterns as our measurements of COS (Fig. 4). Mass-independent sulfur anomalies in sulfate and sulfide minerals and Martian meteorites are likely created in the terrestrial and Martian paleoatmospheres during photodissociation of

SO_2 released by volcanic activities (Farquhar et al., 2000; Savarino et al., 2003). Multiple photochemistry experiments have been conducted on SO_2 at various wavelengths (100-350 nm), producing S^0 residues associated with positive $\Delta^{33}S$ and negative $\Delta^{36}S$ values (Fig. S4, (Farquhar et al., 2001; Whitehill and Ono, 2012; Whitehill et al., 2015). However, SO_2 was probably not very abundant in the solar nebula (Pasek et al., 2005) or in the Solar System's parent molecular cloud (Tieftrunk et al., 1994) and therefore is unlikely to be responsible for the COS sulfur isotopic anomalies.

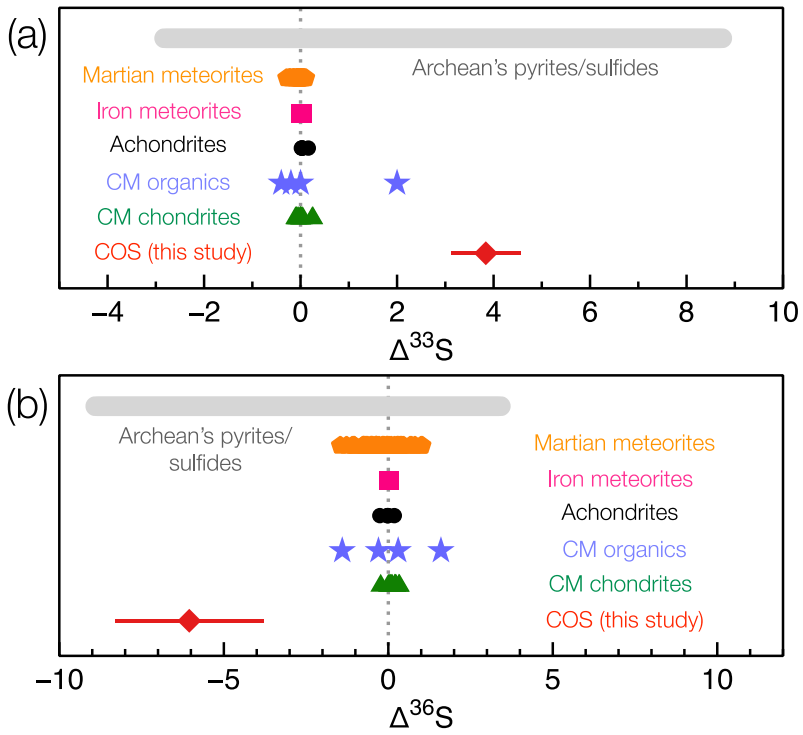

Fig. 4 Range and weighted mean of $\Delta^{33}S$ values (a) and $\Delta^{36}S$ values (b) for COS (two standard errors), terrestrial pyrites and sulfides from Neoarchean rocks (Farquhar et al., 2013; Lin et al., 2018 and references therein), Martian meteorites (Franz et al., 2014; Tomkins et al., 2020), magmatic iron meteorites (Antonelli et al., 2014), achondrites (Rai et al., 2005), CM chondrites (Labidi et al., 2017), and organic sulfonic acids extracted from Murchison (Cooper et al., 1997).

4.3 Irradiation of H_2S from the protosun and massive stars

Hydrogen sulfide is the major sulfur-bearing species in the solar nebular and molecular clouds (Pasek et al., 2005; Rivière-Marichalar et al., 2019). The H_2S photochemistry is, therefore, a possible mechanism to produce the sulfur isotopic signature of COS. The small ^{33}S excesses and ^{36}S depletions reported in achondritic and magmatic iron meteorites (Fig. 4) argue for photochemical reactions of H_2S from Lyα photons in the inner solar nebula (Rai,

2005; Antonelli et al., 2014). On the other hand, larger mass-independent sulfur isotope anomalies extracted from organic sulfonic acids and inorganic sulfur compounds in CM chondrites (Fig. 4) rather suggest that H_2S photolysis more likely took place in the outer solar nebula or in the Solar System's parent molecular cloud by interstellar UV (Cooper et al., 1997; Labidi et al., 2017), which is produced mainly by massive O and B stars (Parravano et al., 2003).

Since UV photolysis by the protosun or by O and B stars may be able to produce mass-independent sulfur anomalies, we calculated the expected $\Delta^{36}S/\Delta^{33}S$ ratios generated from these two scenarios to compare with our measured $\Delta^{36}S/\Delta^{33}S$ ratios in COS. We used the UV spectrum of LkCa 15 (a 1−2 Myr old, 0.9 $M_{\odot}$, T Tauri star with 89% of its 91-317 nm UV flux in the Lyα emission line (Table 4) as an analogous spectrum for the young Sun (Fig. 5). For the interstellar UV spectrum, we compared with two radiation fields: *(i)* the standard interstellar radiation field (Draine, 1978) and its extension (van Dishoeck and Black, 1982) (Fig. 5a), which represents the bulk UV spectrum average for stars in the Galaxy dominated by the UV from O and B stars and *(ii)* a 20,000 K blackbody spectrum to replicate a typical B-type star (which have temperatures between 10,000 and 20,000 K) (Fig. 5b) (Heays et al., 2017). These massive stars are hot enough to have no significant emission lines in this part of the spectrum. All the spectra have been normalized to agree with the integrated flux of the interstellar radiation field of Draine (1978). We also tested alternative interstellar radiation fields from Habing (1968) and Mathis et al., (1983) for comparison (Fig. 5a and Table 4).

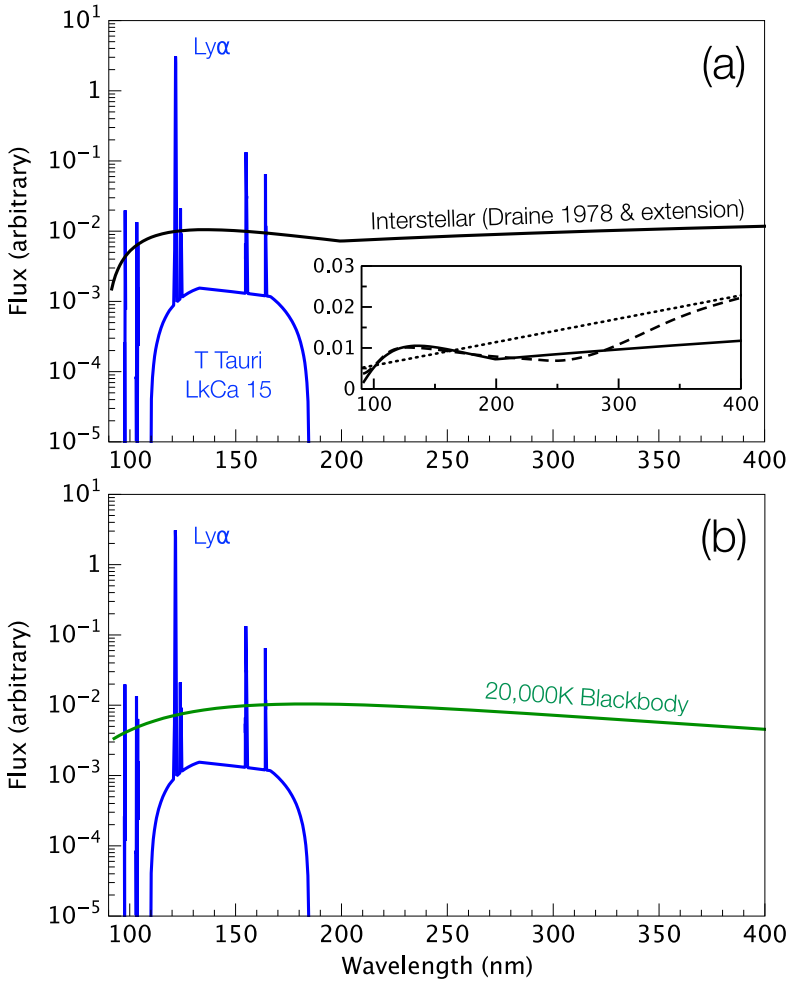

Fig. 5 Ultraviolet spectra of the T Tauri LkCa 15 (France et al., 2014) along with (a) the interstellar UV radiation field (Draine, 1978) and its extension (van Dishoeck and Black, 1982) and (b) a 20,000 K blackbody radiation field (B-type star) (Heays et al., 2017). The inset figure shows the alternative interstellar radiation fields that were also tested in our model (dashed line: (Mathis et al., 1983), dotted line: (Habing, 1968).

Then, using *(i)* the LkCa 15, Draine (1978) and the 20,000 K blackbody UV spectra (Fig. 5), *(ii)* the photodissociation cross sections of H_2S (Fig. 6a, Heays et al., 2017) and *(iii)* the $\Delta^{36}S$ vs. $\Delta^{33}S$ slopes from H_2S photolysis experimental data at different wavelengths (Fig. 6b, Farquhar et al., 2000; Chakraborty et al., 2013), we calculated the expected $\Delta^{36}S$ vs. $\Delta^{33}S$ values that result from H_2S photolysis by the young Sun and interstellar UV (Fig. 7 and Table 4). We first calculated weights by multiplying the photodissociation cross section by the UV flux of LkCa 15 and the interstellar or 20,000 K blackbody spectra for each wavelength, from 90 nm to 250 nm. Then, we calculated the $\Delta^{36}S$ vs. $\Delta^{33}S$ values at each of these wavelengths by interpolating between the measured literature values using a smoothed cubic spline (see Supplementary Material S2-S3 for how we calculated slopes, intercepts, and uncertainties from Chakraborty et al. (2013) and Farquhar et al. (2000)).

The isotope anomalies in the H_2S photolysis experiments are likely created by mixing between the five predissociation branches (Chakraborty et al., 2013). Therefore, we expect a smooth variation between the $\Delta^{36}S/\Delta^{33}S$ values at different wavelengths. To interpolate $\Delta^{36}S$ vs. $\Delta^{33}S$ values as a function of wavelength between the measurements, we used Matlab's "fit" function with the "smoothingspline" model and smoothing factor of 0.05. The $\Delta^{36}S$ variances are calculated by propagating errors for the linear fit (including correlated errors) of $\Delta^{36}S$ vs. $\Delta^{33}S$ for each measured wavelength. The inverse variances are used as weights for the spline fit. We chose the spline smoothing factor to balance between a smooth variation between $\Delta^{36}S/\Delta^{33}S$ values (Fig. 6b) and to generally reproduce the experimental $\Delta^{36}S/\Delta^{33}S$ uncertainties. The $\Delta^{36}S$ vs. $\Delta^{33}S$ values for each spectrum were then calculated as a weighted mean of the $\Delta^{36}S$ vs. $\Delta^{33}S$ values using the above-described weights. We employed a Monte Carlo bootstrap approach to calculate the uncertainty in these slopes (see Supplementary Material for Matlab code).

We estimated uncertainties in the $\Delta^{36}S$ vs. $\Delta^{33}S$ models for each spectrum as follows. Using the experimentally measured $\Delta^{36}S$ and $\Delta^{33}S$ values for each wavelength, we calculated 10,000 bootstrap replicates of the data, using a Gaussian random number generator (Matlab's normrnd) parameterized by the data and associated uncertainties. Following the Monte Carlo procedure described in (Mahon, 1996), we fit a line to each of these replicates using total weighted least squares (Krystek and Anton, 2011). A histogram of the 10,000 slopes generated by this procedure can be skewed or have higher tails than a Gaussian. To account for this non-Gaussian shape, we fit a Stable distribution (also called a Lévy alpha-stable distribution) to the 10,000 slopes (Supplementary Materials, Fig. S12). This yields an error distribution of the $\Delta^{36}S$ vs. $\Delta^{33}S$ values for each wavelength. Since the $\Delta^{36}S$ and $\Delta^{33}S$ wavelength data are not strictly proportional (we allow for an offset from the origin), we calculate the error distribution for 100 $\Delta^{33}S$ values between −2 and +5. For each experimentally measured wavelength and $\Delta^{33}S$ value, we then draw a random $\Delta^{36}S$ value given by the error distribution calculated in the previous step. We then re-interpolate between these six values using the same procedure (smoothed cubic spline) described above. Then we used the same process as described above to compute new $\Delta^{36}S$ vs. $\Delta^{33}S$ values for each spectrum. We calculated 100,000 of these resampled $\Delta^{36}S$ vs. $\Delta^{33}S$ values for each spectrum and calculated the 2.275 and 97.725 percentiles of these values to estimate the 95.45% confidence interval (i.e., $\pm 2\sigma$) of the model $\Delta^{36}S$ vs. $\Delta^{33}S$ values. Figure 6b shows modeled $\Delta^{36}S/\Delta^{33}S$ uncertainties. The data at 139.1 nm is much more uncertain than 121.6 nm and 157 nm wavelengths, which causes the smoothed spline to underpredict the spread in $\Delta^{36}S/\Delta^{33}S$

values at 139.1 nm at the expense of overestimating the spread at 121.6 and 157 nm. Because of small offsets from the origin in the experimental $\Delta^{36}S$ vs. $\Delta^{33}S$ data (see Supplementary Material), the spectrum models do not go exactly through the origin. However, the $\Delta^{36}S$ intercept is close to zero for the spectrum models, so we can parameterize each spectrum model with the $\Delta^{36}S/\Delta^{33}S$ ratio and its uncertainty. More photolysis experiments in the 90−310 nm range will improve our understanding of the physics behind mass-independent fractionation of H_2S and allow for more accurate and precise models in the future.

For comparison, we also calculated the $\Delta^{36}S/\Delta^{33}S$ ratios resulting from SO_2 photolysis by the young Sun and interstellar UV (Fig. S5). The model assumes an initial composition of $\Delta^{33,36}S = 0$ for the H_2S gas as suggested by the non-mass-independent isotopic compositions of sulfides in Acfer 094 (Fig. 3a and Table 3) and in carbonaceous chondrites (e.g., Bullock et al., 2010).

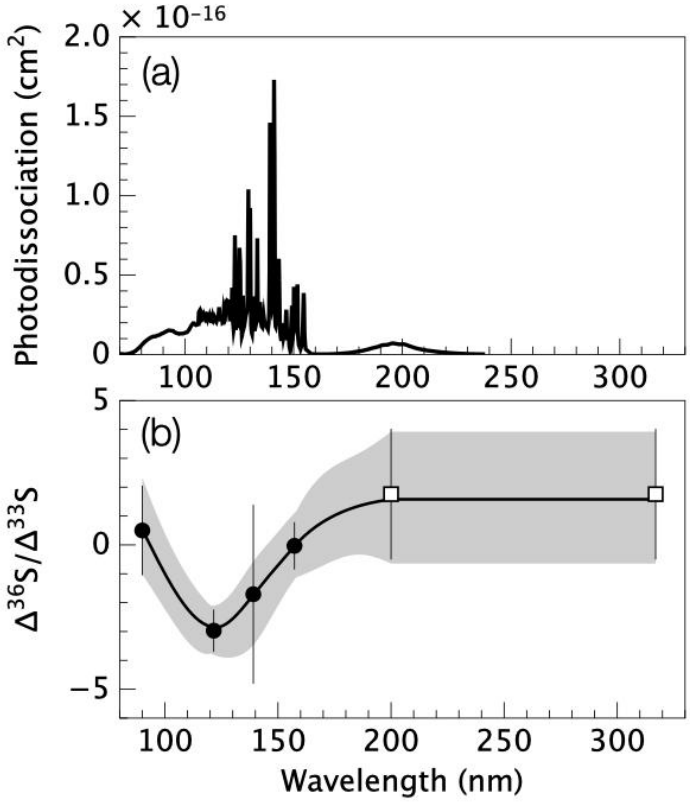

Fig. 6 (a) Photodissociation cross section of H_2S (Heays et al., 2017). (b) Interpolated $\Delta^{36}S/\Delta^{33}S$ values and modeled 2σ uncertainties (grey area) produced during H_2S photodissociation experiments at different wavelengths (90, 121.6, 157.3, 200 and 317 nm). Filled circle: (Chakraborty et al., 2013) and open square: (Farquhar et al., 2001). The $\Delta^{36}S/\Delta^{33}S$ values for wavelengths between the experimentally measured data were interpolated using a smoothed cubic spline (see text for details).

To estimate if the analog young Sun, interstellar UV, or the B-star spectra are consistent with our measured COS anomalies at the 2σ level, we calculated the difference in $\Delta^{36}S/\Delta^{33}S$ between each modeled spectrum and COS at the measured COS $\Delta^{33}S$ value using conditional probabilities and numerical probability density functions of the modeled spectra. LkCa 15, interstellar UV, and the 20,000 K blackbody lie on lines that are well approximated by their $\Delta^{36}S/\Delta^{33}S$ ratios of −2.89 ± 0.84, −1.75 ± 0.71, and −1.53 ± 0.67 (2σ), respectively (Fig. 7a−b). Our measured $\Delta^{36}S/\Delta^{33}S$ for COS is −1.58 (weighted mean) with an uncertainty of 0.66 (two standard errors of the weighted mean). The 2σ allowed confidence interval of the difference between COS $\Delta^{36}S/\Delta^{33}S$ and the $\Delta^{36}S/\Delta^{33}S$ created by UV from LkCa 15 (the modeled young Sun) is [0.18, 2.50] (COS−LkCa15), between COS and the interstellar UV is [−0.78, 1.14] (COS−IS), and between COS and a 20,000 K blackbody is [-0.97, 0.91] (COS-20K).

Our measured COS mean value is, therefore, inconsistent with photochemical processing by the Sun's UV at >2σ confidence but is consistent with irradiation from the interstellar UV or a B star (Fig. 7a−b). We ran a similar analysis using our model for SO_2 photodissociation and found that the $\Delta^{36}S/\Delta^{33}S$ ratios for both interstellar and protosun scenarios are highly inconsistent with our COS data (Table 4).

The $\Delta^{36}S/\Delta^{33}S$ value generated by a given T Tauri star depends most strongly on the fraction of its UV spectrum close to the Lyα wavelength (Fig. 6). Other T Tauri stars, such as the solar-mass T Tauri star LkCa 15, have a larger fraction of their ~100-300 nm flux near the Lyα wavelength compared to LkCa 15, and so would have a lower $\Delta^{36}S/\Delta^{33}S$ than LkCa 15. This would consequently increase the difference between the modeled protosun $\Delta^{36}S/\Delta^{33}S$ and the interstellar $\Delta^{36}S/\Delta^{33}S$. We calculated $\Delta^{36}S$ vs. $\Delta^{33}S$ for fifteen T Tauri stars to test whether the model results using these spectra are consistent with our measured COS $\Delta^{36}S/\Delta^{33}S$ (Table 4). We found that H_2S photolysis by UV from 13 of the 15 T Tauri stars are inconsistent with our COS measurements at just above the 2σ confidence level (the confidence interval of the difference between COS and the modeled spectrum does not overlap zero), and 2 of the 15 T Tauri stars (those with the smallest Lyα fraction) differ from COS equal to or just below the 2σ confidence level (Table 4).

The S^0 products for 121.6 nm photolysis define arrays in $\delta^{33}S$ vs. $\delta^{34}S$ that have a shallower slope than the MDF line (Chakraborty et al., 2013). The $\delta^{36}S$ vs. $\delta^{34}S$ arrays for 121.6 nm are steeper than the mass-dependent fractionation line. The ratio of the differences in the slopes of these lines compared to the mass-dependent fractionation line yields a

$\Delta^{36}S/\Delta^{33}S$ value for each wavelength. The S^0 products for 121.6 nm have positive $\delta^{34}S$ values, and therefore positive $\Delta^{36}S$ values and negative $\Delta^{33}S$ values (Fig. 7a–b). Our measured COS grains have the complementary composition: negative $\Delta^{36}S$ and positive $\Delta^{33}S$ values and have larger isotope anomalies than the experiments. The astrophysics environment that we propose for COS formation differs greatly from the experiments of Chakraborty et al. (2013): UV flux, gas densities, and irradiation times are all very different and impossible to simulate in the laboratory. The most fundamental physics results of the Chakraborty et al. (2013) experiments are the $\delta^{33}S$ vs. $\delta^{34}S$ and $\delta^{36}S$ vs. $\delta^{34}S$ slopes: the magnitudes of the produced anomalies may not be relevant to cosmochemical environments. Additionally, the direction of products (S^0) and residues (H_2S) may be inherited by different mechanisms from different Solar System bodies: the sulfur isotope anomalies in iron meteorites measured by Antonelli et al., (2014) were proposed to be inherited from either residues or products of ~2% total disk H_2S photolysis by the young Sun in the inner Solar System (at ~1 AU). The magnitude and sign of the $\Delta^{36}S$ vs. $\Delta^{33}S$ isotope anomalies inherited by COS are difficult to interpret. However, the $\Delta^{36}S/\Delta^{33}S$ value is the critical signature and can be used to constrain the formation of COS in an astrophysical environment.

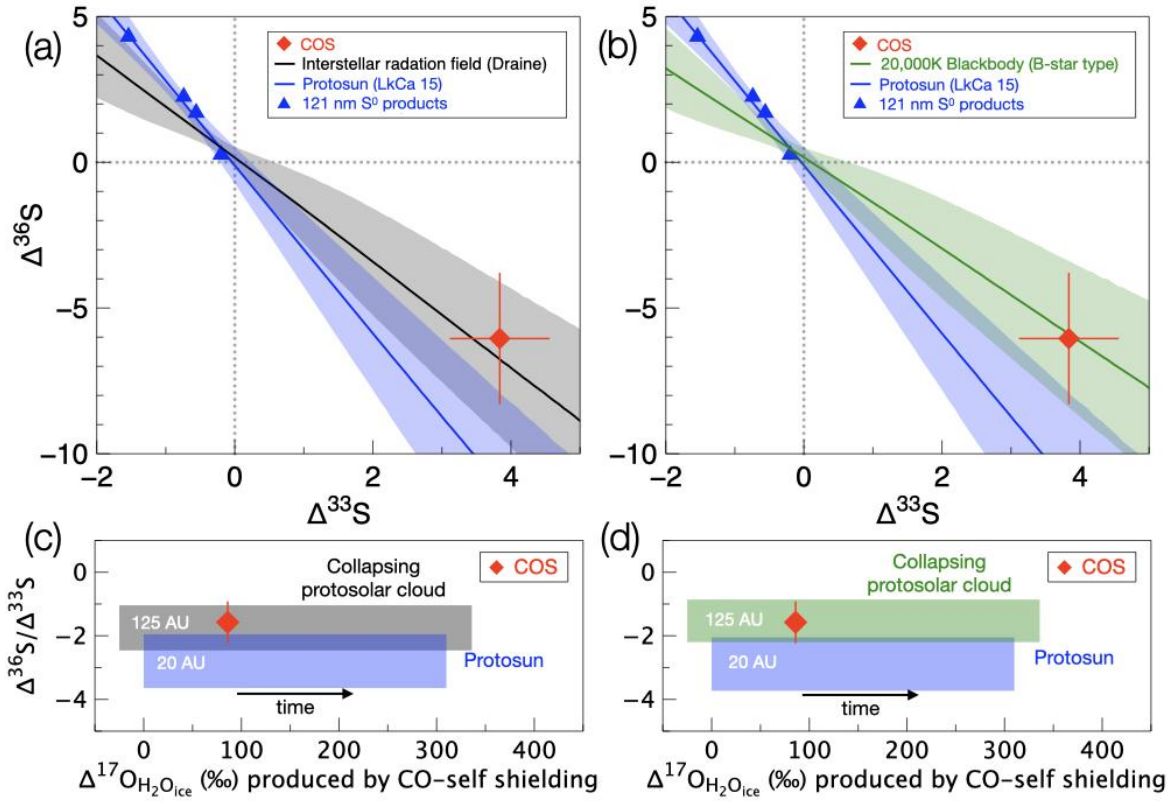

Fig. 7 $\Delta^{36}S$ vs. $\Delta^{33}S$ plot showing the expected slopes with 2σ confidence bands from H_2S photolysis by the young Sun (LkCa 15 spectrum) and (a) interstellar UV (Draine 1987 and extension) and (b) a B-type star (20,000 K blackbody, Heays et al., 2017) compared to the

weighted mean and two standard errors of the measured COS grains. Experimental S^0 photodissociation products at Lyα (121 nm) are also shown (Chakraborty et al., 2013) and lie along a similar line ($\Delta^{36}S$ vs. $\Delta^{33}S$ slopes of -2.97 ± 0.73, 2σ) as the modeled protosun. (b) Measured $\Delta^{36}S/\Delta^{33}S$ vs. $\Delta^{17}O$ of COS grains in Acfer 094 (weighted means and two standard errors) compared to models of photochemical anomalies produced by the young Sun (blue band) and interstellar UV (c) from Draine (1987) (grey band), and (d) from a B-type star (green band). The vertical height of each band is the model $\Delta^{36}S/\Delta^{33}S$ value ± 2σ model uncertainty, calculated as described in the text.

While our sulfur isotope data favor a UV source from massive stars over the protosun, it does not specify where the photochemical processing occurred. A possibly valid scenario is that our measured sulfur and oxygen isotope anomalies originated in the outer solar nebula (Lyons and Young, 2005; Young, 2007b), where the low surface densities of gas and dust allowed UV from a nearby massive star to penetrate in the disk and dominate the UV flux over the protosun itself (Hester and Desch, 2005; Ciesla and Sandford, 2012). Such a scenario is possible, because calculations show that *(i)* massive stars could possibly coexist in a stellar cluster of a few hundred stars with the protosun (Gounelle, 2015) and *(ii)* examples of protoplanetary disks being photoevaporated by massive stars, known as proplyds, are seen in the Orion Nebula (Hester and Desch, 2005). However, recent measurements of $\Delta^{17}O$ variations in the earliest (^{26}Al-poor) CAIs show that the solar nebula likely inherited oxygen isotope anomalies from the molecular cloud, as CO self-shielding after the Sun's formation (by the Sun or nearby massive stars) cannot act fast enough to produce these anomalies in the nebula (Krot et al., 2020). Figure 7b shows the $\Delta^{36}S/\Delta^{33}S$ and $\Delta^{17}O$ values of COS compared to models of photochemical anomalies produced by the young Sun and interstellar UV. The horizontal range of the blue band is the range in $\Delta^{17}O$ of water ice produced during CO self-shielding via irradiation from the protosun in the nebula (Young, 2007b), and that from nearby stars in the collapsing protosolar cloud is shown by the grey bar (Lee et al., 2008). In the protosun irradiation model, CO photodissociation by the young Sun in the outer solar nebula produces a time-dependent ^{16}O depletion peak up to $\Delta^{17}O \approx +310‰$ for H_2O_{ice} at 20 AU. The model assumes a dust size of 3 μm, an accretion rate of 10^{-7} $M_\odot yr^{-1}$, and a FUV flux from the central star of 5×10^3 times the local interstellar flux (see (Young, 2007b) for details). The horizontal range of the grey band denotes the range in $\Delta^{17}O$ of water ice produced by CO self-shielding by nearby stars (Lee et al., 2008). This process yields a maximum time-dependent anomaly of $\Delta^{17}O \approx +335‰$ at 125 AU (assuming an interstellar radiation field of $\times10^5$ times the local interstellar field; see Lee et al., 2008 for details). Either

the protosun or interstellar models could predict the $\Delta^{17}O$ value of COS that we measured, and only the interstellar model is consistent with the measured $\Delta^{36}S/\Delta^{33}S$ of COS. The coupled mass-independent sulfur and oxygen isotopic anomalies in COS, further imply that the formation of these anomalies took place in the same astrophysical environment. Therefore, although photodissociation in the outer solar nebula cannot be totally ruled out, we conclude that it is less likely than a molecular cloud origin.

4.4 H_2S photolysis in molecular clouds and implications for the Sun's birthplace

Many gas-phase sulfur species have been detected in cold molecular clouds, such as SO, SO_2 and H_2S, but their total abundance in these environments appears to be depleted by a factor of ~1,000 relative to the sulfur cosmic abundance (Tieftrunk et al., 1994). It has been proposed that most of the sulfur is locked inside the icy mantles of dust particles, in the form of $H_2S_{(ice)}$. However, H_2S ice has not been detected so far in icy mantles since its main absorption bands are hindered by those of methanol (CH_3OH), a major component of interstellar ices (Garozzo et al., 2010). Hydrogen sulfide can be efficiently formed on the surface of dust grains by hydrogenation of sulfur atoms at low temperatures (Jiménez-Escobar and Caro, 2011). Subsequently, $H_2S_{(ice)}$ is exposed to strong UV and/or ion irradiation in molecular clouds and photodissociates. Irradiation experiments have shown that pure irradiated H_2S ice photolyzes rapidly into several sulfur species, including HS, H_2S_2, S_2 and S_3 (Jiménez-Escobar and Caro, 2011). In the presence of H_2O ice, irradiation of mixed H_2O-H_2S ice leads to the formation of more oxidized S-bearing species, including SO_2, SO_4^{2-} and HSO_4^-. While irradiation of H_2S ice in cold molecular clouds is a possible scenario to create sulfur isotopic anomalies in interstellar ice, there are currently no experiments that have shown a mass-independent sulfur isotope anomaly can be produced this way. Therefore, more H_2O-H_2S ice irradiation experiments coupled with sulfur isotope characterization are needed to address the feasibility of this mechanism.

Alternatively, a likely environment to produce sulfur isotope anomalies in gas-phase H_2S is photodissociation regions (PDRs) where nearby massive stars irradiate the edges of cold molecular clouds, such as the Pillars of Creation in the Eagle Nebula (Fig. 8a−b, Mizuta et al., 2008). In PDRs, the gas reaches a higher temperature (~100−1,000 K) than the dust (~50−100 K), and both temperatures gradually decrease toward the molecular cloud's center (Goicoechea et al., 2017). At $T_{dust} \gtrsim 70$ K, H_2S will sublimate from icy mantles on dust grains to the gas-phase (Fig. 8c). Ultraviolet light from these nearby massive stars will

665 photodissociate ~75% (Zhou et al., 2020) of the remaining $H_2S_{(gas)}$ into SH (in the excited
666 $A^2\Sigma^+$ state) or S^0 and create isotope anomalies in the product S and residual H_2S. If $T_{gas} \gtrsim 370$
667 K (Seto et al. 2008), photochemically produced S^0 would be converted back to H_2S by
668 reaction with H_2, no mass-independent sulfur reservoir would be created (Labidi et al., 2017).
669 At $T_{gas} \approx 70–370$ K, photochemically produced S^0 will adsorb onto molecular cloud dust
670 grains (Fig. 8c). Subsequently, condensed S^0 will become $H_2S_{(ice)}$ by hydrogenation, and
671 mass-independent sulfur isotopic anomalies could be preserved in the icy mantles of dust
672 grains (Jiménez-Escobar and Caro, 2011). In order to explain the coexistence of both mass-
673 independent oxygen and sulfur isotope anomalies recorded in COS, CO self-shielding will
674 also take place at the edge of the molecular cloud (Sheffer et al., 2002), producing ^{16}O-poor
675 $H_2O_{(ice)}$ condensed as icy mantles on $H_2S_{(ice)}$-bearing dust grains at $T \leq 170$ K (Fig. 8b). The
676 PDR at the perimeter of the Solar System's parent molecular cloud is, therefore, a plausible
677 environment to reproduce the oxygen and sulfur mass-independent isotope anomalies
678 recorded in COS.
679

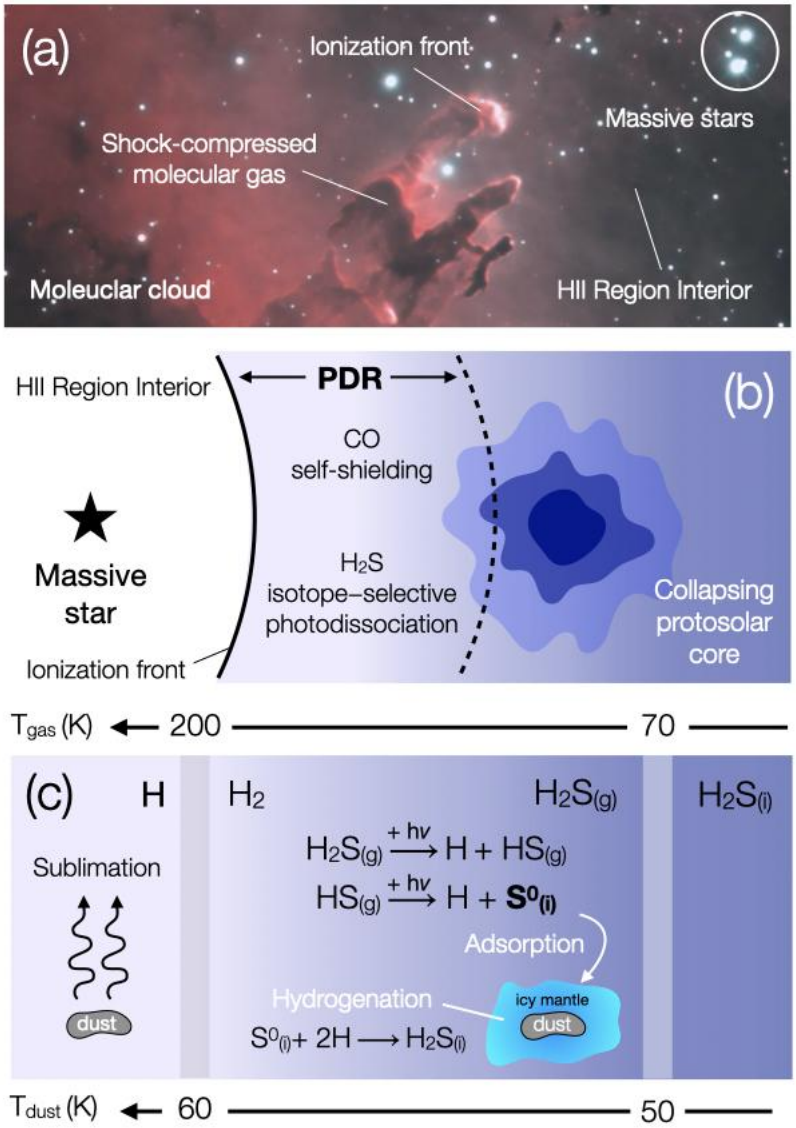

Fig. 8 (a) Optical image (combination of Hydrogen-alpha and Oxygen-II filters) of the Eagle Nebula (M16) and the Pillars of Creation; (image credit: National Geographic Society and annotations from Hester and Desch, 2005). (b) Schematic representation of the formation of a photodissociation region (PDR) into the surrounding molecular cloud exposed to intense UV from a nearby massive star. (c) Schematic representation of the internal structure of the PDR. Dust and gas temperatures from (Esplugues et al., 2019).

During the collapse of the Solar System's parent molecular cloud, ice-mantled dust grains carrying isotope anomalies (produced at the cloud's edge) lag behind and are deposited at the outer edge of the solar nebula (Lee et al., 2008). This dust-hosted isotopically anomalous ice reservoir eventually spreads into the inner Solar System by gas drag. The signature of large oxygen isotope anomalies produced by efficient CO self-shielding in the molecular cloud is reflected in the $\Delta^{17}O$ difference between planetary materials and the Sun (McKeegan et al., 2011). Photochemical processing of H_2S was likely less efficient and produced smaller

anomalies than that of CO, which is reflected by the comparatively narrower range of mass-independent sulfur isotope anomalies in planetary materials (Chakraborty et al., 2013). The undiluted, isotopically anomalous, sulfur-bearing ice reservoir was accreted by some outer Solar System bodies, such as the parent body of Acfer 094.

The sulfur and oxygen isotope measurements seen in COS most likely indicate that the Solar System formed in a large stellar cluster with massive stars (type O and B) in its vicinity. This is a plausible scenario for the Sun's birth environment, since *(i)* the majority of low-mass Sun-like stars form in large clusters with relatively close proximity with massive stars (Hester and Desch, 2005; Adams, 2010) and *(ii)* the presence of short-lived radionuclides at the inferred abundances (e.g., ^{26}Al) in meteorites provides evidence that the Sun formed in a typical massive-star-forming region (Gounelle and Meynet, 2012; Young, 2018).

5. CONCLUSIONS

We measured large mass-independent isotope anomalies in oxygen and sulfur in cosmic symplectite (COS), a magnetite-sulfide symplectic assemblage, in the ungrouped carbonaceous chondrite Acfer 094. Given the mineralogical texture of COS, the observed mass-independent isotope anomalies are mostly likely caused by photochemical processing of H_2S gas. Furthermore, our measured $\Delta^{36}S/\Delta^{33}S$ anomalies are inconsistent with UV irradiation of gaseous H_2S by the young Sun (with significant Lyman-alpha radiation from neutral hydrogen) but are consistent with irradiation of H_2S by nearby massive stars (without a significant Lyman-alpha component). We propose that in Acfer 094's icy parent body anomalous sulfur-bearing ices combined with anomalous water ice, both of which created by photochemistry of gas-phase molecules in the molecular cloud. The sulfur and oxygen isotope measurements seen in COS most likely indicate that the Solar System formed in a large stellar cluster with at least one massive star (type O or B) in its vicinity.

This is a plausible scenario for the Sun's birth environment, since *(i)* the majority of low-mass Sun-like stars form in large clusters with relatively close proximity with massive stars (Hester and Desch, 2005; Adams, 2010), possibly from a previous generation of star formation, and *(ii)* the presence of short-lived radionuclides (e.g., ^{26}Al) in meteorites provides evidence that the Sun formed in a typical massive-star-forming region (Gounelle and Meynet, 2012; Young, 2018).

Declaration of Competing Interest

The authors declare that they have no known competing financial interests or personal relationships that could have appeared to influence the work reported in this paper.

Acknowledgments

The authors wish to thank the Smithsonian National Museum of Natural History for providing the section of Acfer 094 analyzed in this study. The authors are grateful to J. Lewis and T. Smolar for assistance with NanoSIMS analyses, and to S. Desch, K. Lodders, and B. Fegley for helpful discussions. We thank Larry Nittler and an anonymous reviewer for constructive comments and helpful discussions on the model, and Sasha Krot for efficient editorial handling. Funding: This work was supported by the McDonnell Center for Space Sciences at Washington University in St. Louis, and NASA grant NNX14AF22G (RCO). This work has made use of the CTTS FUV high-resolution ultraviolet radiation field database.

Research data

Original data of this study are available in the supplementary file.

Tables

Table 1. Oxygen isotopic composition of COS from Acfer 094.

Sample	$^{16}O^{-}$ (c/s)	$\delta^{18}O$ (‰)	2σ	$\delta^{17}O$ (‰)	2σ	$\Delta^{17}O$ (‰)	2σ
COS1	6.7×10^4	174	6	182	18	91	19
COS2	6.0×10^4	156	6	163	18	82	19
COS3	1.4×10^5	170	6	164	17	76	18
COS4	1.1×10^5	196	6	193	17	91	18
COS5	1.2×10^5	187	6	186	17	89	18
COS6	1.1×10^5	173	6	190	17	100	18
COS7	1.3×10^5	183	6	172	17	77	18
COS8	1.5×10^5	192	6	184	18	84	19
Weighted Mean		**179**		**179**		86	
2 standard errors		*8*		*8*		*6*	

$$\Delta^{17}O = \delta^{17}O - 0.52 \times \delta^{18}O$$

Table 2. Sulfur isotopic composition of COS using the scanning ion imaging mode.

Sample	$^{32}S^-$ (c/px/s)	$\delta^{34}S$ (‰)	2σ	$\delta^{33}S$ (‰)	2σ	$^{36}S^-$ (c/px/s)	$\delta^{36}S$ (‰)	2σ	$\Delta^{33}S$	2σ	$\Delta^{36}S$	2σ
COS12	3.35×10^5	8.05	2.33	8.68	3.12	2.35×10^2	10.53	5.07	4.54	4.42	-4.73	5.57
COS11	1.95×10^5	10.00	1.71	7.05	2.01	2.85×10^2	18.01	4.75	1.91	2.84	-0.98	5.04
COS1	2.33×10^5	13.88	1.13	10.75	2.16	1.60×10^2	19.56	6.38	3.63	3.06	-6.84	6.47
COS5	1.84×10^5	14.05	1.42	10.09	1.94	1.11×10^2	21.82	4.86	2.88	2.75	-4.90	5.05
*COS4	1.96×10^5	14.75	1.07	11.48	2.43	–	–	–	3.91	3.44	–	–
COS10	2.01×10^5	14.95	1.74	14.02	3.16	1.59×10^2	21.52	7.66	6.35	4.48	-6.92	7.84
COS8	1.64×10^5	15.19	1.68	11.36	1.91	9.21×10^1	20.73	6.84	3.57	2.70	-8.17	7.04
COS3	2.56×10^5	15.92	1.73	12.97	3.49	1.55×10^2	22.08	7.08	4.81	4.94	-8.21	7.28
COS2	2.57×10^5	16.24	1.30	11.65	2.44	1.41×10^2	30.56	5.81	3.32	3.45	-0.36	5.94
COS6	1.93×10^5	18.95	1.69	13.60	2.89	1.12×10^2	26.00	7.56	3.88	4.10	-10.12	7.73
COS7	2.07×10^5	19.59	1.91	15.26	2.45	1.09×10^2	26.29	5.74	5.22	3.48	-11.06	6.03
Weighted mean	**2.20×10^5**	**14.79**		**11.34**		**1.56×10^2**	**21.40**		**3.84**		**-6.05**	
2 standard errors	*2.89×10^4*	*2.03*		*1.44*		*3.85×10^1*	*3.41*		*0.72*		*2.25*	

$$\Delta^{33}S = \delta^{33}S - 1000 \times [(1 + \delta^{34}S / 1000)^{0.515} - 1].$$

$$\Delta^{36}S = \delta^{36}S - 1000 \times [(1 + \delta^{34}S / 1000)^{1.89} - 1].$$

"–" denotes discarded values.

* $^{36}S/^{34}S$ ratio of COS4 was discarded because the B-field value of the $^{36}S^-$ peak centering was off compared to the bracketed standards.

760 **Table 3.** Sulfur isotopic composition of pyrrhotites in Acfer 094 (ungrouped) and Murchison
761 (CM2) using the spot mode and the scanning ion imaging mode for comparison.

Spot mode											
Sample	**$^{32}S^{-}$ (c/s)**	**$\delta^{34}S$ (‰)**	**2σ**	**$\delta^{33}S$ (‰)**	**2σ**	**$\delta^{36}S$ (‰)**	**2σ**	**$\Delta^{33}S$**	**2σ**	**$\Delta^{36}S$**	**2σ**
ACF094-S2	1.71×10^{8}	-5.58	0.67	-2.83	0.93	-12.07	2.74	0.04	1.00	-1.50	1.48
ACF094-S7	1.81×10^{8}	-3.30	0.82	-1.12	1.18	-4.65	2.99	0.58	1.25	1.61	2.40
ACF094-S6	1.83×10^{8}	-2.99	0.57	-1.57	0.61	-5.17	2.57	-0.03	0.68	0.51	1.02
ACF094-S1	1.72×10^{8}	-1.40	0.56	-0.18	0.72	-2.81	2.62	0.54	0.78	-0.16	1.00
MURC-S2	2.37×10^{8}	-9.71	0.87	-5.29	0.86	-16.80	3.39	-0.28	0.97	1.58	2.95
MURC-S4	2.05×10^{8}	-5.76	0.82	-2.80	0.87	-9.75	3.53	0.18	0.96	1.17	2.66
MURC-S1	1.87×10^{8}	-2.37	0.82	-0.78	0.92	-6.62	3.56	0.44	1.01	-2.13	2.68
Scanning ion imaging mode											
Sample	**$^{32}S^{-}$ (c/px/s)**	**$\delta^{34}S$ (‰)**	**2σ**	**$\delta^{33}S$ (‰)**	**2σ**	**$\delta^{36}S$ (‰)**	**2σ**	**$\Delta^{33}S$**	**2σ**	**$\Delta^{36}S$**	**2σ**
ACF094-S8	3.32×10^{5}	-0.31	1.00	0.17	1.76	1.11	5.07	0.33	1.83	1.70	5.41

762
763

Table 4. List of the expected $\Delta^{36}S/\Delta^{33}S$ values calculated from our model for H_2S photodissociation for different UV spectra: T Tauri stars, interstellar radiation fields, and 20,000 K blackbody. The 2σ confidence interval (COS-UV) for H_2S photodissociation represents the difference between the $^{36}S/\Delta^{33}S$ ratio calculated from the $\Delta^{33}S$ and $\Delta^{36}S$ weighted means of COS (−1.58) and associated two standard errors (0.66), and the calculated $\Delta^{36}S$ vs. $\Delta^{33}S$ values and associated 2σ uncertainties for each spectrum.

UV spectrum	Mass ($M_\odot$)	Lyα fraction[a]	$\Delta^{36}S/\Delta^{33}S$ (H_2S)	2σ	2σ confidence COS−UV spectrum[b]	$\Delta^{36}S/\Delta^{33}S$ (SO_2)	2σ
T Tauri star							
BP Tau	0.7	0.40	-2.68	0.79	[0.03, 2.22]	4.09	0.59
DE Tau	0.6	0.87	-2.87	0.84	[0.17, 2.48]	4.29	0.64
DF Tau	0.2	0.88	-2.92	0.86	[0.20, 2.55]	4.32	0.66
DM Tau	0.5	0.84	-2.86	0.84	[0.17, 2.47]	4.28	0.63
DR Tau	0.8	0.44	-2.42	0.79	[-0.22, 1.95]	4.05	0.55
GM Aur	1.2	0.80	-2.83	0.83	[0.14, 2.43]	4.26	0.64
HN Tau	0.9	0.80	-2.84	0.83	[0.15, 2.44]	4.26	0.64
LkCa 15	0.9	0.89	-2.89	0.84	[0.18, 2.50]	4.30	0.65
RECX 11	0.8	0.89	-2.89	0.85	[0.18, 2.50]	4.30	0.65
RECX 15	0.4	0.96	-2.93	0.86	[0.21, 2.56]	4.34	0.66
RU Lupi	0.8	0.28	-2.62	0.78	[-0.02, 2.16]	4.02	0.60
SU Aur	1.7	0.87	-2.88	0.84	[0.17, 2.49]	4.29	0.65
TW Hya	0.8	0.58	-2.66	0.78	[0.01, 2.21]	4.10	0.60
UX Tau	1.3	0.92	-2.90	0.85	[0.19, 2.52]	4.31	0.65
V 4046 Sgr	0.9	0.91	-2.91	0.85	[0.20, 2.53]	4.30	0.64
Interstellar radiation field and 20,000 K blackbody							
Habing 1968		0.00	-1.46	0.62	[-1.00, 0.80]	2.07	0.17
Mathis et al., 1983		0.01	-1.74	0.69	[-0.78, 1.14]	2.57	0.19
Draine 1987		0.01	-1.75	0.71	[-0.78, 1.18]	2.62	0.20
20,000 K blackbody		0.01	-1.53	0.67	[-0.97, 0.91]	2.24	0.18

The T Tauri star UV spectra are taken from (France et al., 2014).
The interstellar UV radiation fields are taken from (Heays et al., 2017).
[a] Lyman-α fractions were estimated in the wavelength range of 91.2 to 317.0 nm.

REFERENCES

Abe K., Sakamoto N., Krot A. N. and Yurimoto H. (2017) Occurrences, abundances, and compositional variations of cosmic symplectites in the Acfer 094 ungrouped carbonaceous chondrite. *Geochem. J.* **51**, 3–15.

Adams F. C. (2010) The birth environment of the Solar System. *Annu. Rev. Astron. Astrophys.* **48**, 47–85.

Antonelli M. A., Kim S.-T., Peters M., Labidi J., Cartigny P., Walker R. J., Lyons J. R., Hoek J. and Farquhar J. (2014) Early inner solar system origin for anomalous sulfur isotopes in differentiated protoplanets. *Proc. Natl. Acad. Sci.* **111**, 17749–17754.

Bullock E. S., Gounelle M., Lauretta D. S., Grady M. M. and Russell S. S. (2005) Mineralogy and texture of Fe-Ni sulfides in CI1 chondrites: Clues to the extent of aqueous alteration on the CI1 parent body. *Geochim. Cosmochim. Acta* **69**, 2687–2700.

Bullock E. S., McKeegan K. D., Gounelle M., Grady M. M. and Russell S. S. (2010) Sulfur isotopic composition of Fe-Ni sulfide grains in CI and CM carbonaceous chondrites: Fe-Ni sulfides in CI and CM chondrites. *Meteorit. Planet. Sci.* **45**, 885–898.

Calmonte U., Altwegg K., Balsiger H., Berthelier J. J., Bieler A., Cessateur G., Dhooghe F., van Dishoeck E. F., Fiethe B., Fuselier S. A., Gasc S., Gombosi T. I., Hässig M., Le Roy L., Rubin M., Sémon T., Tzou C.-Y. and Wampfler S. F. (2016) Sulphur-bearing species in the coma of comet 67P/Churyumov–Gerasimenko. *Mon. Not. R. Astron. Soc.* **462**, S253–S273.

Chakraborty S., Jackson T. L., Ahmed M. and Thiemens M. H. (2013) Sulfur isotopic fractionation in vacuum UV photodissociation of hydrogen sulfide and its potential relevance to meteorite analysis. *Proc. Natl. Acad. Sci.* **110**, 17650–17655.

Ciesla F. J. and Sandford S. A. (2012) Organic Synthesis via Irradiation and Warming of Ice Grains in the Solar Nebula. *Science* **336**, 452.

Clayton R. N. (1979) Isotopic anomalies in the early solar system. *Proc. Second Symp.* **11**, 121–125.

Clayton R. N. (2002) Self-shielding in the solar nebula. *Nature* **415**, 860–861.

Cooper G. W., Thiemens M. H., Jackson T. L. and Chang S. (1997) Sulfur and Hydrogen Isotope Anomalies in Meteorite Sulfonic Acids. *Science* **277**, 1072.

Crowe D. E. and Vaughan R. G. (1996) Characterization and use of isotopically homogeneous standards for in situ laser microprobe analysis of 34S/32 S ratios. *Am. Mineral.* **81**, 187–193.

Ding T., Valkiers S., Kipphardt H., Bièvre P. D., Taylor P. D. P., Gonfiantini R. and Krouse R. (2001) Calibrated sulfur isotope abundance ratios of three IAEA sulfur isotope reference materials and V-CDT with a reassessment of the atomic weight of sulfur. *Geochim. Cosmochim. Acta* **65**, 2433–2437.

van Dishoeck E. F. and Black J. (1982) The excitation of interstellar C2. *Astrophys. J.* **258**,

533–547.

Draine B. T. (1978) Photoelectric heating of interstellar gas. *Astrophys. J. Suppl. Ser.* **36**, 595–619.

Esplugues G., Cazaux S., Caselli P., Hocuk S. and Spaans M. (2019) Dust temperature and time-dependent effects in the chemistry of photodissociation regions. *Mon. Not. R. Astron. Soc.* **486**, 1853–1874.

Farquhar J., Cliff J., Zerkle A. L., Kamyshny A., Poulton S. W., Claire M., Adams D. and Harms B. (2013) Pathways for Neoarchean pyrite formation constrained by mass-independent sulfur isotopes. *Proc. Natl. Acad. Sci.* **110**, 17638.

Farquhar J., Savarino J., Airieau S. and Thiemens M. H. (2001) Observation of wavelength-sensitive mass-independent sulfur isotope effects during SO_2 photolysis: Implications for the early atmosphere. *J. Geophys. Res. Planets* **106**, 32829–32839.

Farquhar J., Savarino J., Jackson T. L. and Thiemens M. H. (2000) Evidence of atmospheric sulphur in the martian regolith from sulphur isotopes in meteorites. *Nature* **404**, 50–52.

Floss C., Stadermann F. J., Kearsley A. T., Burchell M. J. and Ong W. J. (2013) The abundance of presolar grains in comet 81P/WILD 2. *Astrophys. J.* **763**, 140.

France K., Schindhelm E., Bergin E. A., Roueff E. and Abgrall H. (2014) High-resolution ultraviolet radiation fields of classical T Tauri stars. *Astrophys. J.* **784**, 127.

Franz H. B., Kim S.-T., Farquhar J., Day J. M. D., Economos R. C., McKeegan K. D., Schmitt A. K., Irving A. J., Hoek J. and III J. D. (2014) Isotopic links between atmospheric chemistry and the deep sulphur cycle on Mars. *Nature* **508**, 364–368.

Gao X. and Thiemens M. H. (1991) Systematic study of sulfur isotopic composition in iron meteorites and the occurrence of excess 33S and 36S. *Geochim. Cosmochim. Acta* **55**, 2671–2679.

Garozzo M., Fulvio D., Kanuchova Z., Palumbo M. E. and Strazzulla G. (2010) The fate of S-bearing species after ion irradiation of interstellar icy grain mantles. *Astron. Astrophys.* **509**, A67.

Goicoechea J. R., Cuadrado S., Pety J., Aguado A., Black J. H., Bron E., Cernicharo J., Chapillon E., Fuente A., Gerin M. and al et (2017) The ALMA view of UV-irradiated cloud edges: unexpected structures and processes. *Proc. Int. Astron. Union* **13**, 210–217.

Gounelle M. (2015) The abundance of ^{26}Al-rich planetary systems in the Galaxy. *Astron. Astrophys.* **582**, A26.

Gounelle M. and Meynet G. (2012) Solar system genealogy revealed by extinct short-lived radionuclides in meteorites. *Astron. Astrophys.* **545**, A4.

Guillou C. L. and Brearley A. (2014) Relationships between organics, water and early stages of aqueous alteration in the pristine CR3.0 chondrite MET 00426. *Geochim.*

Cosmochim. Acta **131**, 344–367.

Habing H. (1968) The interstellar radiation density between 912 A and 2400 A. *Bull. Astron. Inst. Neth.* **19**, 421.

Harries D. and Langenhorst F. (2013) The nanoscale mineralogy of Fe,Ni sulfides in pristine and metamorphosed CM and CM/CI-like chondrites: Tapping a petrogenetic record. *Meteorit. Planet. Sci.* **48**, 879–903.

Heays A. N., Bosman A. D. and van Dishoeck E. F. (2017) Photodissociation and photoionisation of atoms and molecules of astrophysical interest. *Astron. Astrophys.* **602**, A105.

Hester J. J. and Desch S. J. (2005) Understanding Our Origins: Star Formation in HII Region Environments. In *Chondrites and the Protoplanetary Disk* (eds. A. N. Krot, E. R. D. Scott, and B. Reipurth). Astronomical Society of the Pacific Conference Series. p. 107.

Hoppe P., Rubin M. and Altwegg K. (2018) Presolar Isotopic Signatures in Meteorites and Comets: New Insights from the Rosetta Mission to Comet 67P/Churyumov–Gerasimenko. *Space Sci. Rev.* **214**, 106.

Jacquet E., Pignatale F. C., Chaussidon M. and Charnoz S. (2019) Fingerprints of the Protosolar Cloud Collapse in the Solar System. II. Nucleosynthetic Anomalies in Meteorites. *Astrophys. J.* **884**, 32.

Jiménez-Escobar A. and Caro G. M. M. (2011) Sulfur depletion in dense clouds and circumstellar regions I. H_2S ice abundance and UV-photochemical reactions in the H2O-matrix. *Astron. Astrophys.* **536**, A91.

Kimura M., Grossman J. N. and Weisberg M. K. (2011) Fe-Ni metal and sulfide minerals in CM chondrites: An indicator for thermal history. *Meteorit. Planet. Sci.* **46**, 431–442.

Kimura M., Grossman J. N. and Weisberg M. K. (2008) Fe-Ni metal in primitive chondrites: Indicators of classification and metamorphic conditions for ordinary and CO chondrites. *Meteorit. Planet. Sci.* **43**, 1161–1177.

Krot A. N., McKeegan K. D., Huss G. R., Liffman K., Sahijpal S., Hutcheon I. D., Srinivasan G., Bischoff A. and Keil K. (2006) Aluminum-Magnesium and Oxygen Isotope Study of Relict Ca-Al-rich Inclusions in Chondrules. *Astrophys. J.* **639**, 1227–1237.

Krot A. N., Nagashima K., Lyons J. R., Lee J.-E. and Bizzarro M. (2020) Oxygen isotopic heterogeneity in the early Solar System inherited from the protosolar molecular cloud. *Sci. Adv.* **6**, eaay2724.

Krystek M. and Anton M. (2011) A least-squares algorithm for fitting data points with mutually correlated coordinates to a straight line. *Meas. Sci. Technol.* **22**, 035101.

Labidi J., Farquhar J., Alexander C. M. O., Eldridge D. L. and Oduro H. (2017) Mass independent sulfur isotope signatures in CMs: Implications for sulfur chemistry in the early solar system. *Geochim. Cosmochim. Acta* **196**, 326–350.

Lee J.-E., Bergin E. A. and Lyons J. R. (2008) Oxygen isotope anomalies of the Sun and the original environment of the solar system. *Meteorit. Planet. Sci.* **43**, 1351–1362.

Leroux H., Cuvillier P., Zanda B. and Hewins R. H. (2015) GEMS-like material in the matrix of the Paris meteorite and the early stages of alteration of CM chondrites. *Geochim. Cosmochim. Acta* **170**, 247–265.

Lin M., Zhang X., Li M., Xu Y., Zhang Z., Tao J., Su B., Liu L., Shen Y. and Thiemens M. H. (2018) Five-S-isotope evidence of two distinct mass-independent sulfur isotope effects and implications for the modern and Archean atmospheres. *Proc. Natl. Acad. Sci.* **115**, 8541–8546.

Lyons J. R. (2014) Photodissociation of CO isotopologues: Models of laboratory experiments and implications for the solar nebula. *Meteorit. Planet. Sci.* **49**, 373–393.

Lyons J. R. and Young E. D. (2005) CO self-shielding as the origin of oxygen isotope anomalies in the early solar nebula. *Nature* **435**, 317–320.

Mahon K. I. (1996) The New "York" Regression: Application of an Improved Statistical Method to Geochemistry. *Int. Geol. Rev.* **38**, 293–303.

Mathis J. S., Mezger P. G. and Panagia N. (1983) Interstellar radiation field and dust temperatures in the diffuse interstellar matter and in giant molecular clouds. *Astron Astrophys* **128**, 212–229.

Matsumoto M., Tsuchiyama A., Nakato A., Matsuno J., Miyake A., Kataoka A., Ito M., Tomioka N., Kodama Y., Uesugi K., Takeuchi A., Nakano T. and Vaccaro E. (2019) Discovery of fossil asteroidal ice in primitive meteorite Acfer 094. *Sci. Adv.* **5**, eaax5078.

McKeegan K. D., Kallio A. P. A., Heber V. S., Jarzebinski G., Mao P. H., Coath C. D., Kunihiro T., Wiens R. C., Nordholt J. E., Moses R. W., Reisenfeld D. B., Jurewicz A. J. G. and Burnett D. S. (2011) The Oxygen Isotopic Composition of the Sun Inferred from Captured Solar Wind. *Science* **332**, 1528.

Mizuta A., Kane J., Pound M., Remington B., Ryutov D. and Takabe H. (2008) Formation of Pillars at the Boundaries between H II Regions and Molecular Clouds. *Astrophys. J.* **647**, 1151.

Nguyen A. N., Berger E. L., Nakamura- Messenger K., Messenger S. and Keller L. P. (2017) Coordinated mineralogical and isotopic analyses of a cosmic symplectite discovered in a comet 81P/Wild 2 sample. *Meteorit. Planet. Sci.* **52**, 2004–2016.

Palmer E. E. and Lauretta D. S. (2011) Aqueous alteration of kamacite in CM chondrites: Kamacite alteration in CM chondrites. *Meteorit. Planet. Sci.* **46**, 1587–1607.

Parravano A., Hollenbach D. J. and McKee C. F. (2003) Time Dependence of the Ultraviolet Radiation Field in the Local Interstellar Medium. *Astrophys. J.* **584**, 797–817.

Pasek M., Milsom J., Ciesla F., Lauretta D., Sharp C. and Lunine J. (2005) Sulfur chemistry with time-varying oxygen abundance during Solar System formation. *Icarus* **175**, 1–14.

Rai V. K. (2005) Photochemical Mass-Independent Sulfur Isotopes in Achondritic Meteorites. *Science* **309**, 1062–1065.

Rai V. K., Jackson T. L. and Thiemens M. H. (2005) Photochemical Mass-Independent Sulfur Isotopes in Achondritic Meteorites. *Science* **309**, 1062–1065.

Rivière-Marichalar P., Fuente A., Goicoechea J. R., Pety J., Le Gal R., Gratier P., Guzmán V., Roueff E., Loison J. C., Wakelam V. and Gerin M. (2019) Abundances of sulphur molecules in the Horsehead nebula: First NS^+ detection in a photodissociation region. *Astron. Astrophys.* **628**, A16.

Rowe M. W., Clayton R. N. and Mayeda T. K. (1994) Oxygen isotopes in separated components of CI and CM meteorites. *Geochim. Cosmochim. Acta* **58**, 5341–5347.

Sakamoto N., Seto Y., Itoh S., Kuramoto K., Fujino K., Nagashima K., Krot A. N. and Yurimoto H. (2007) Remnants of the Early Solar System Water Enriched in Heavy Oxygen Isotopes. *Science* **317**, 231–233.

Savarino J., Romero A., Cole-Dai J., Bekki S. and Thiemens M. H. (2003) UV induced mass-independent sulfur isotope fractionation in stratospheric volcanic sulfate. *Geophys. Res. Lett.* **30**.

Schnieder L., Meier W., Welge K. H., Ashfold M. N. R. and Western C. M. (1990) Photodissociation dynamics of H_2S at 121.6 nm and a determination of the potential energy function of SH (A 2Σ+). *J. Chem. Phys.* **92**, 7027–7037.

Schrader D. L., Davidson J. and McCoy T. J. (2016) Widespread evidence for high-temperature formation of pentlandite in chondrites. *Geochim. Cosmochim. Acta* **189**, 359–376.

Seto Y., Sakamoto N., Fujino K., Kaito T., Oikawa T. and Yurimoto H. (2008) Mineralogical characterization of a unique material having heavy oxygen isotope anomaly in matrix of the primitive carbonaceous chondrite Acfer 094. *Geochim. Cosmochim. Acta* **72**, 2723–2734.

Sheffer Y., Lambert D. L. and Federman S. R. (2002) Ultraviolet Detection of Interstellar $^{12}C^{17}O$ and the CO Isotopomeric Ratios toward X Persei. *Astrophys. J.* **574**, L171–L174.

Simon J. I., Ross D. K., Nguyen A. N., Simon S. B. and Messenger S. (2019) Molecular Cloud Origin for Oxygen Isotopic Heterogeneity Recorded by a Primordial Spinel-rich Refractory Inclusion. *Astrophys. J.* **884**, L29.

Singerling S. A. and Brearley A. J. (2020) Altered primary iron sulfides in CM2 and CR2 carbonaceous chondrites: Insights into parent body processes. *Meteorit. Planet. Sci.* **55**, 496–523.

Smith R. L., Pontoppidan K. M., Young E. D., Morris M. R. and Dishoeck E. F. van (2009) High-Precision $C^{17}O$, $C^{18}O$, and $C^{16}O$ Measurements in Young Stellar Objects: Analogues for CO Self-Shielding in The Early Solar System. *Astrophys. J.* **701**, 163–175.

969 Thalmann C., Grady C. A., Goto M., Wisniewski J. P., Janson M., Henning T., Fukagawa M.,
970 Honda M., Mulders G. D., Min M., Moro-Martín A., McElwain M. W., Hodapp K.
971 W., Carson J., Abe L., Brandner W., Egner S., Feldt M., Fukue T., Golota T., Guyon
972 O., Hashimoto J., Hayano Y., Hayashi M., Hayashi S., Ishii M., Kandori R., Knapp G.
973 R., Kudo T., Kusakabe N., Kuzuhara M., Matsuo T., Miyama S., Morino J.-I.,
974 Nishimura T., Pyo T.-S., Serabyn E., Shibai H., Suto H., Suzuki R., Takami M.,
975 Takato N., Terada H., Tomono D., Turner E. L., Watanabe M., Yamada T., Takami
976 H., Usuda T. and Tamura M. (2010) Imaging of a transitional disk gap in reflected
977 might: indications of planet formation around yhe young solar analog LkCa 15.
978 *Astrophys. J.* **718**, L87–L91.

979 Thiemens M. H. and Lin M. (2019) Use of Isotope Effects to Understand the Present and Past
980 of the Atmosphere and Climate and Track the Origin of Life. *Angew. Chem. Int. Ed.*
981 **58**, 6826–6844.

982 Tieftrunk A., Forets G., Schilke P. and Walmsley C. (1994) SO and H_2S in low density
983 molecular clouds. *Astron. Astrophys.* **289**, 579–596.

984 Tomkins A. G., Alkemade S. L., Nutku S. E., Stephen N. R., Finch M. A. and Jeon H. (2020)
985 A small S-MIF signal in Martian regolith pyrite: Implications for the atmosphere.
986 *Geochim. Cosmochim. Acta*.

987 Vacher L. G., Ogliore R. C., Liu N., Nagashima K. and Huss G. R. (2020) Accretion and
988 Circulation of ^{16}O-Poor Water in the Acfer 094 Parent Body. In 51st Lunar and
989 Planetary Science Conference. Lunar and Planetary Institute, The Woodlands, Texas.
990 p. Abstract #2495.

991 Vacher L. G., Piralla M., Gounelle M., Bizzarro M. and Marrocchi Y. (2019) Thermal
992 Evolution of Hydrated Asteroids Inferred from Oxygen Isotopes. *Astrophys. J.* **882**,
993 L20.

994 Whitehill A. R., Jiang B., Guo H. and Ono S. (2015) SO_2 photolysis as a source for sulfur
995 mass-independent isotope signatures in stratospehric aerosols. *Atmospheric Chem.*
996 *Phys.* **15**, 1843–1864.

997 Whitehill A. R. and Ono S. (2012) Excitation band dependence of sulfur isotope mass-
998 independent fractionation during photochemistry of sulfur dioxide using broadband
999 light sources. *Geochim. Cosmochim. Acta* **94**, 238–253.

1000 Young E. D. (2007a) Strange Water in the Solar System. *Science* **317**, 211.

1001 Young E. D. (2018) The birth environment of the solar system constrained by the relative
1002 abundances of the solar radionuclides. *Proc. Int. Astron. Union* **14**, 70–77.

1003 Young E. D. (2007b) Time-dependent oxygen isotopic effects of CO self shielding across the
1004 solar protoplanetary disk. *Earth Planet. Sci. Lett.* **262**, 468–483.

1005 Yurimoto H. and Kuramoto K. (2004) Molecular Cloud Origin for the Oxygen Isotope
1006 Heterogeneity in the Solar System. *Science* **305**, 1763.

1007 Zhou J., Zhao Y., Hansen C. S., Yang J., Chang Y., Yu Y., Cheng G., Chen Z., He Z., Yu S.,
1008 Ding H., Zhang W., Wu G., Dai D., Western C. M., Ashfold M. N. R., Yuan K. and

1009 Yang X. (2020) Ultraviolet photolysis of H2S and its implications for SH radical
1010 production in the interstellar medium. *Nat. Commun.* **11**, 1547.

1011 Zolensky M. E., Ivanov A. V., Yang S. V., Mittlefehldt D. W. and Ohsumi K. (1996) The
1012 Kaidun meteorite: Mineralogy of an unusual CM1 lithology. *Meteorit. Planet. Sci.* **31**,
1013 484–493.

1014 Zolensky M. E. and Thomas K. L. (1995) Iron and iron-nickel sulfides in chondritic
1015 interplanetary dust particles. *Geochim. Cosmochim. Acta* **59**, 4707–4712.

1016